

Speckle Decorrelation in Fundamental and Second-Harmonic Light Scattered from Nonlinear Disorder

Rabisankar Samanta,¹ Romain Pierrat^{2,*}, Rémi Carminati^{2,3} and Sushil Mujumdar^{1,†}

¹*Nano-Optics and Mesoscopic Optics Laboratory, Tata Institute of Fundamental Research, 1 Homi Bhabha Road, Mumbai 400 005, India*

²*Institut Langevin, ESPCI Paris, PSL University, CNRS, 1 rue Jussieu, Paris 75005, France*

³*Institut d'Optique Graduate School, Université Paris-Saclay, Palaiseau F-91127, France*



(Received 31 July 2022; accepted 5 October 2022; published 16 November 2022)

Speckle patterns generated in a disordered medium carry a lot of information despite the apparent complete randomness in the intensity pattern. When the medium possesses $\chi^{(2)}$ nonlinearity, the speckle is sensitive to the phase of the incident fundamental light, as well as the light generated within. Here, we examine the speckle decorrelation in the fundamental and second-harmonic transmitted light as a function of the varying power in the fundamental beam. At low incident powers, the speckle patterns produced by successive pulses exhibit strong correlations, which decrease with increasing power. The average correlation in the second-harmonic speckle decays faster than in the fundamental speckle. Next, we construct a theoretical model, backed up by numerical computations, to obtain deeper physical insights into the faster decorrelations in the second-harmonic light. While providing excellent qualitative agreement with the experiments, the model sheds light on the contribution of two effects in the correlations, namely, the generation of second-harmonic light and the propagation thereof.

DOI: [10.1103/PhysRevApplied.18.054047](https://doi.org/10.1103/PhysRevApplied.18.054047)

I. INTRODUCTION

Wave transport in a random medium is a universal phenomenon that transcends the boundaries of various subtopics, such as optics, condensed-matter physics, acoustics, quantum matter, etc. [1]. Among all of these, the transport of optical waves has attracted the most attention due to the sophisticated experimental capabilities offered by optics. Indeed, the study of photon transport through disordered media has revealed important facets of transport in all regimes of disorder, from weak scattering occurring in media such as fog to strong scattering in dense powders. With increasing disorder, incident waves experience multiple scattering, where the transport of intensity is described as a diffusion process. Further increase in disorder leads to exotic phenomena such as weak localization and strong localization manifest in the system, which essentially represent reduced or arrested photon transport [2]. Traditionally, all these phenomena have been studied in the linear regime due to the inherent noninteracting nature of photons. However, interactions can be created by introducing nonlinearities into the media. Materials that respond to higher powers of incident electric fields can be

exploited to create disordered systems that favor nonlinear propagation. The consequences of nonlinearity on the physics of light transport in disorder have been extensively addressed both in $\chi^{(3)}$ media, which are media exhibiting intensity-dependent refractive index [3–6], and in $\chi^{(2)}$ media, which can generate second-harmonic frequencies of light [7–14]. In the latter scenario, research efforts have been focused on the fundamental physics of diffusion and weak localization in $\chi^{(2)}$ disorder [7,8,10,11] and on the applicability of disorder in enhancing nonlinear generation [12–14].

One of the most fundamental effects of disorder that depends on the phase of the propagating light is the appearance of speckles. A speckle pattern is the random intensity distribution of bright and dark spots developed due to the interference of many coherent wavelets with the same frequency and different amplitudes and phases traveling in a disordered medium [15]. Despite the apparent complete randomness in the intensity distribution, various correlations [16] are known to exist in the speckle pattern. For instance, the optical-memory effect “remembers” the incoming wave front under slight perturbation in position and angle [17–21], an idea that has emerged as an efficient tool in imaging through opaque media [22,23]. Recent theory and experiments have unveiled non-Gaussian and long-range correlations between transmitted and reflected speckle patterns [24–26]. Not surprisingly, the rich physics

*romain.pierrat@espci.psl.eu

†mujumdar@tifr.res.in

of speckle correlations has already motivated research in nonlinear systems. For instance, a nonlinear optical-memory effect [27] has been revealed in a $\chi^{(3)}$ medium, namely a silica aerogel, through a series of pump and probe experiments wherein a disordered medium is agitated by an optothermal nonlinearity. Another well-known consequence of $\chi^{(3)}$ nonlinearity is speckle instability, wherein the speckle pattern fluctuates and becomes unstable when the nonlinearity surpasses a threshold value [28–30]. In the weak-localization regime, the speckle patterns formed by nonlinear point scatterers exhibit dynamic instability and lead to chaotic behavior of the system [31]. Such speckle instabilities in $\chi^{(3)}$ nonlinear disordered media have been experimentally reported [32]. On the other hand, $\chi^{(2)}$ nonlinearity has been employed to primarily investigate angular correlations in speckles. For example, experiments and calculations have shown that angular correlations in the reflected speckle scale with the sample thickness for second-harmonic light, in contrast to scaling with the mean free path for fundamental light [33]. In another study [34], angular correlations in second-harmonic speckle under dual-beam excitation have been presented in a medium of LiNbO_3 microcrystals.

In this paper, we report our experimental and theoretical studies on intensity-dependent decorrelation in speckle patterns produced by a second-order nonlinear disordered medium. Specifically, we show that the fundamental and second-harmonic speckle patterns produced by successive incident pulses exhibit strong correlations at low input power, which drop at higher power. The correlation between fundamental speckle patterns remains high compared to the second harmonic. The decay rate of the average correlation with increasing power is larger in the second-harmonic speckles than in the fundamental speckles. To understand the decorrelation process, we build a theoretical model that traces the propagation of the linear field, followed by the conversion to the second harmonic, and finally followed by the propagation of the second harmonic. The model is in excellent qualitative agreement with the experimental results. The theoretical model is also backed up by a Monte Carlo computation, which sheds light on two contributions to the decorrelation process, namely, the decorrelation during the generation of the second harmonic and that due to the propagation thereof.

II. EXPERIMENTS

A. Experimental setup

In preparation for the experiment, commercially available KDP (potassium dihydrogen phosphate, EMSURE ACS) crystal grains are adopted as our nonlinear material. Initially, the grain sizes range from approximately 2 mm to 3 mm and are uneven in shape. The grains are subjected to a ball-milling process, creating a fine powder of KDP, with particle sizes ranging from 2 to 8 μm .

The distribution of grain sizes approximately follows a log-normal distribution, with a peak at 3.11 μm and a variance of 1.25 μm . For the speckle measurement, we prepare two opaque slabs (thickness approximately $510 \pm 15 \mu\text{m}$ and approximately $680 \pm 20 \mu\text{m}$) of KDP microcrystals and the slabs are sandwiched between two microscopic slides of thickness approximately $170 \pm 5 \mu\text{m}$. A coherent backscattering (CBS) [35,36] experiment estimates the transport mean free path (ℓ_t) of the slabs and the estimated values are approximately 352 μm and 169 μm at $\lambda = 1064 \text{ nm}$ and $\lambda = 532 \text{ nm}$, respectively. Figure 1 illustrates a schematic of the experimental setup for the speckle-correlations measurements.

Nd:YAG laser pulses (EKSPLA, PL2143B, pulse width approximately 30 ps) with a fundamental wavelength of $\lambda = 1064 \text{ nm}$ (hereafter referred to as IR), are chosen as our input beam. A glass wedge is introduced in the incident path to direct a small fraction (approximately 4%) of the beam to a power meter (PM, Ophir Optonics, resolution 10 μW) for the input-power measurement. The residual beam is then focused onto the scattering medium (SM) through a lens (L) of focal length 10 cm. To avoid damage to the sample, it is placed slightly away from the focus. The transmitted light consists of both the fundamental and second-harmonic light (here referred to as SHG, $\lambda = 532 \text{ nm}$). A harmonic beam splitter (HBS) is employed to separate the two components. The transmitted (IR) and reflected (SHG) light from the HBS is then directed to CCD1 and CCD2, respectively. CCD1 is an (In, Ga)As detector (SWIR camera, Photonic Science, UK) with pixel dimension $30 \mu\text{m} \times 30 \mu\text{m}$, while CCD2 is a silicon detector (iXon Ultra 897, Andor technology) with pixel dimension $16 \mu\text{m} \times 16 \mu\text{m}$. A laser line filter (F1) at $\lambda = 1064 \text{ nm}$ is added in front of CCD1 to block any unwanted SHG photons. Similarly, a laser line filter (F2) at $\lambda = 532 \text{ nm}$ is placed in front of CCD2. The laser fires at a repetition rate of 1 Hz and simultaneous measurements of the pulse power and the corresponding IR and SHG speckle patterns are made.

B. Results

An intense pulse of laser light impacts the disordered sample and imparts a certain radiation pressure, which causes the particles to be displaced from their original position. Overall, the disorder configuration at the input face is modified, in proportion to the pump power. See Appendix A for more details. Since the disorder configuration changes with every impacting optical pulse, it is imperative to avoid cumulative reconfigurations happening through multiple pump pulses. Therefore, we only grab two successive speckle patterns in two consecutive pump pulses and then translate the sample so as to illuminate a different location on the sample. The homogeneity of the disorder strength is constant across the total area, as also

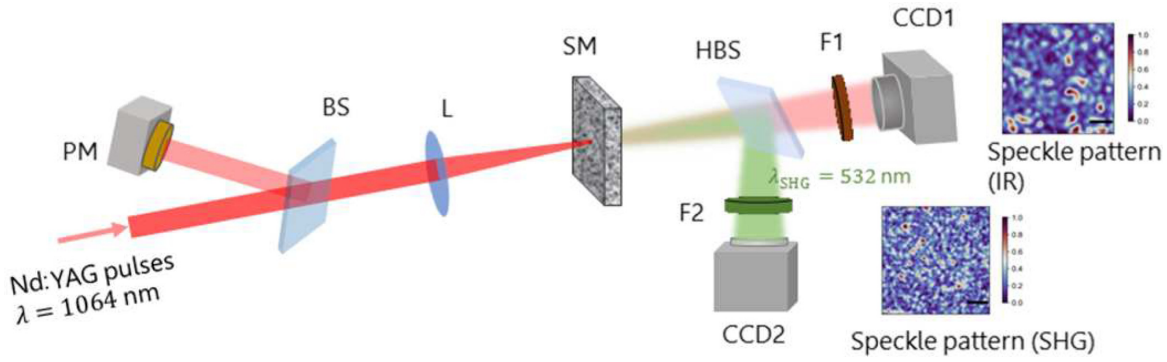


FIG. 1. A schematic of the experimental setup: BS, beam splitter; PM, power meter; L, lens; SM, scattering medium; HBS, harmonic beam splitter; F1, laser line filter at $\lambda = 1064$ nm; F2, laser line filter at $\lambda = 532$ nm; CCD1, charge-coupled device with (In, Ga)As detector; CCD2, charged-coupled device with silicon detector. Two experimental speckle patterns for fundamental (hereafter referred to as IR, $\lambda = 1064$ nm) and second-harmonic generated (hereafter referred to as SHG, $\lambda = 532$ nm) light are shown here, while the adjacent color bars indicate the normalized intensity scale.

certified by the systematic variation in the results. The correlation coefficient between two speckle patterns A and B (both $m \times n$ matrices) is calculated as

$$C_{\text{expe}} = \frac{\sum_{i=1}^m \sum_{j=1}^n (A_{ij} - \bar{A})(B_{ij} - \bar{B})}{\sqrt{\left(\sum_{i=1}^m \sum_{j=1}^n (A_{ij} - \bar{A})^2\right) \left(\sum_{i=1}^m \sum_{j=1}^n (B_{ij} - \bar{B})^2\right)}}, \quad (1)$$

where the overbar represents the mean of the matrix.

The initial two consecutive speckle patterns of IR and SHG light at an input power of 10.5 mW are presented in Figs. 2(a)–2(d), respectively. Obvious agreement is seen between Fig. 2(a) and Fig. 2(b), with the yellow circles emphasizing the regions of clear similarity. For the SHG wavelength, there are no similarities in the speckle patterns between two consecutive pulses, indicating strong decorrelation within two pulses. The correlation coefficient $\langle C_{\text{expe}} \rangle$ is averaged over ten sets of speckle patterns, each grabbed at a different location on the sample at the same pump intensity.

Figure 3 reveals the variant decorrelation with pump power for the fundamental and second-harmonic light. A monotonic decrease in the correlation coefficient is observed in both samples of thicknesses $L = 510 \mu\text{m}$ and $L = 680 \mu\text{m}$. At low powers, up to about 15 mW, the correlation drops rapidly, after which the rate reduces with further increase in power. It can be expected to asymptotically approach zero. To compare the qualitative rate of decorrelation between IR and SHG, we calculate the slopes of the two curves for each point and plot them in Fig. 3(c). For $L = 510 \mu\text{m}$ and IR light, the slope initially drops, indicating a slowing down of the decorrelation with increasing power. Subsequently, it rises monotonically. For the SHG light, an initially static slope is seen to rise monotonically and then saturate at the highest power. For the

thicker sample, the trends are very similar. The intersection between the blue and red curves indicates the pump power at which the decorrelation rates are the same. Evidently, the two curves intersect at a lower pump power for the thicker sample. The slopes of the two curves represent a valuable diagnostic for comparing with the theoretical model, which is discussed later.

The source of the fluctuating speckle pattern can be traced to the radiation pressure of the incident pulses, which induces displacements in the scatterers in random

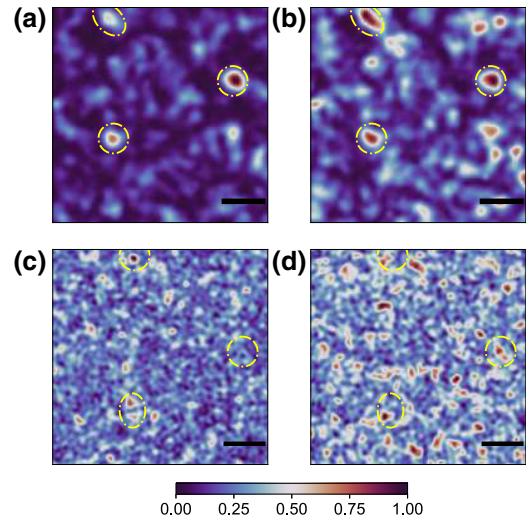


FIG. 2. The initial two consecutive speckle patterns of (a),(b) IR and (c),(d) SHG light scattered from a $510\text{-}\mu\text{m}$ -thick sample at an input power of 10.53 mW. The IR speckle shows higher correlation (0.71) and the marked regions with yellow circles emphasize the agreement. On the contrary, the correlation for SHG light is observed to be low (0.23) and any regions arbitrarily chosen in the pattern (yellow circles) do not show visible agreement. The color bar indicates the normalized intensity. The scale bar represents $600 \mu\text{m}$.

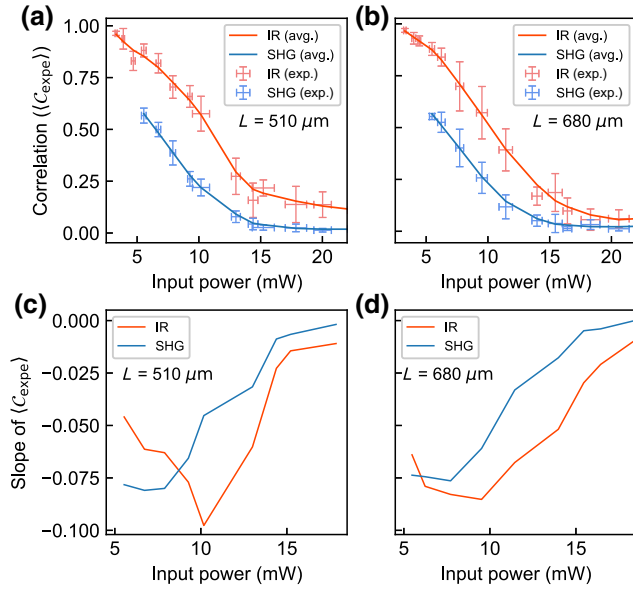


FIG. 3. (a),(b) The correlation coefficient between the first two consecutive speckle patterns of IR (red markers) and SHG (blue markers) light as a function of the input power of the fundamental light, calculated from measured speckle patterns. The solid lines are obtained after smoothing the experimental data. The data are measured on two different samples with thickness (a) $L = 510 \mu\text{m}$ and (b) $L = 680 \mu\text{m}$. (c),(d) The slopes of $\langle C_{\text{expe}} \rangle_{\text{IR}}$ and $\langle C_{\text{expe}} \rangle_{\text{SHG}}$ calculated on each power value for the two samples for (c) $L = 510 \mu\text{m}$ and (d) $L = 680 \mu\text{m}$.

directions. This has been experimentally verified in our earlier study, wherein we have shown a decrease in speckle contrast with pump power [37]. Such a situation of scatterer displacement under radiation pressure in a medium without nonlinearities has been theoretically treated in Ref. [38]. A given absolute displacement of the scatterers amounts to a smaller relative displacement with respect to the wavelength for the IR light, as compared to the SHG light. However, the origin of the behavior of decorrelation seen in Fig. 3 is not obvious and needs to be rigorously evaluated. This is carried out in Sec. III.

III. THEORETICAL MODEL

In parallel to the experiment, we develop a theoretical model based on coupled transport equations for the linear ($\lambda = 1064 \text{ nm}$) and second-harmonic ($\lambda = 532 \text{ nm}$) light. While earlier theoretical treatments have relied on coupled diffusion equations for the linear and second-harmonic light [9], the consequence of scatterer displacement has not been invoked. Our model provides physical insights on the origin of the faster decorrelation for the second-harmonic speckle compared to the decorrelation of the linear speckle. Before deriving the model, we first focus on the correlation

function defined in Eq. (1). It can also be written as

$$C_{\text{expe}} = \frac{\int_{\text{CCD}} \delta I(\mathbf{r}) \delta \tilde{I}(\mathbf{r}) d\mathbf{r}}{\left[\int_{\text{CCD}} \delta I^2(\mathbf{r}) d\mathbf{r} \int_{\text{CCD}} \delta \tilde{I}^2(\mathbf{r}) d\mathbf{r} \right]^{1/2}}, \quad (2)$$

where $\delta I = I - \bar{I}$, I being the intensity, and $\bar{I} = \int_{\text{CCD}} I(\mathbf{r}) d\mathbf{r}$. \tilde{I} denotes the intensity once the scatterers have moved due to radiation pressure. It is important to note that this correlation function does not correspond to the correlation of speckle patterns at different times but measures the correlation between the speckles produced by two slightly different disorder configurations, the scatterer displacements being induced by the radiation-pressure effect. Assuming ergodicity, we can replace the integration over the pixels of the CCD camera with a statistical average over all possible disorder configurations which is denoted by $\langle \cdot \rangle$. Moreover, we consider that the statistical properties of the medium are the same after the displacement of the scatterers, i.e., $\langle I \rangle = \langle \tilde{I} \rangle$. Next, we assume that the field has Gaussian statistics (or, equivalently, that the speckles are fully developed), which is valid in the regime $k_0 \ell_s \gg 1$, $k_0 = \omega/c = 2\pi/\lambda$ being the wave number and ℓ_s being the scattering mean free path. This implies that $\langle \delta I^2 \rangle = \langle I \rangle^2$. The correlation function in Eq. (2) becomes $C_{\text{expe}} \sim C_I - 1$, where

$$C_I(\mathbf{r}) = \frac{\langle I(\mathbf{r}) \tilde{I}(\mathbf{r}) \rangle}{\langle I(\mathbf{r}) \rangle^2}. \quad (3)$$

Finally, we also have $C_I = 1 + |C|^2$, where C is the field-field correlation function given by

$$C(\mathbf{r}) = \frac{\langle E(\mathbf{r}) \tilde{E}^*(\mathbf{r}) \rangle}{\langle E(\mathbf{r}) E^*(\mathbf{r}) \rangle}, \quad (4)$$

E being the electric field and the superscript asterisk (“*”) denoting the complex conjugate. It is important to note that we make the assumption of a scalar field for the sake of simplicity. This can be justified in the multiple-scattering regime, where the field can be considered to be fully depolarized [39]. We finally have

$$C_{\text{expe}} \sim |C|^2. \quad (5)$$

The problem of estimating C_{expe} theoretically now reduces to the computation of C for two different frequencies, i.e., ω for the linear beam and 2ω for the second-harmonic one. The purpose of the following subsections is to develop a transport model for C . We present only the important steps, the full derivation from first principles being described in Appendix B.

A. Disorder model

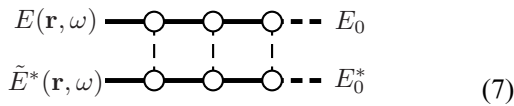
The real samples are composed of packed KDP crystal grains of different sizes and shapes. Thus the most relevant and simple disorder model consists of a fluctuating continuous and real (no absorption) permittivity $\epsilon(\mathbf{r})$. The disorder microstructure is then characterized by a spatial correlation function chosen to be Gaussian, in the form

$$\begin{aligned} C_\epsilon(|\mathbf{r} - \mathbf{r}'|, \omega) &= \langle \delta\epsilon(\mathbf{r}, \omega) \delta\epsilon(\mathbf{r}', \omega) \rangle \\ &= |\Delta\epsilon(\omega)|^2 \exp\left[-\frac{|\mathbf{r} - \mathbf{r}'|^2}{2\ell^2}\right]. \end{aligned} \quad (6)$$

In this equation, $\delta\epsilon(\mathbf{r}, \omega) = \epsilon(\mathbf{r}, \omega) - \langle \epsilon(\mathbf{r}, \omega) \rangle$ is the fluctuating part of the permittivity, $|\Delta\epsilon(\omega)|^2$ is the amplitude of the correlation, and ℓ is the correlation length. $|\Delta\epsilon(\omega)|^2$ depends on frequency, since the permittivity ϵ is dispersive. However, ℓ involves only the geometrical structure of the disorder and thus does not depend on frequency. The $\chi^{(2)}$ nonlinearity is supposed to be correlated in a similar way.

B. Linear regime

We first consider the linear regime ($\lambda = 1064$ nm) corresponding to propagation at the fundamental frequency ω . We use an approach similar to that in Ref. [40], developed in the context of diffusing-wave spectroscopy (DWS). The most important point concerns the selections of the scattering paths followed by the field E and its complex conjugate \tilde{E}^* that dominate in the expression of the correlation function \mathcal{C} . In a dilute medium such that $k_0\ell_s \gg 1$, the leading contribution corresponds to E and \tilde{E}^* following the same scattering sequences. These sequences can be represented by the diagram



with an arbitrary number of scattering events [41]. In these so-called ladder diagrams, the circles represent the scattering events, the thick solid lines correspond to the average Green functions modeling the field propagation between scattering events, and the thick dashed lines denote the incident field. The upper (bottom) line describes the propagation of E (\tilde{E}^*), respectively, and the thin dashed vertical lines represent the disorder correlation C_ϵ . It is important to note that in the model of the continuous disorder, the circles do not represent real scatterers (grains) but scattering events connected by the correlation function C_ϵ . The width ℓ of the correlation function C_ϵ is, however, on the order of the grain size. The ladder shape of this dominant diagram implies that there is always constructive interference between the field E and its complex conjugate \tilde{E}^* . Thus

the problem of computation of \mathcal{C} reduces to the problem of solving a radiative transport equation [42],

$$\begin{aligned} \left[\mathbf{u} \cdot \nabla_{\mathbf{r}} + \frac{1}{\ell_s(\omega)} \right] \tilde{I}(\mathbf{r}, \mathbf{u}, \omega) \\ = \frac{1}{\ell_s(\omega)} \int p(\mathbf{u}, \mathbf{u}', \omega) g(\mathbf{r}, \mathbf{u}, \mathbf{u}', \omega) \tilde{I}(\mathbf{r}, \mathbf{u}', \omega) d\mathbf{u}', \end{aligned} \quad (8)$$

where $\tilde{I}(\mathbf{r}, \mathbf{u}, \omega)$ is the specific intensity, that can be seen as the radiative flux at position \mathbf{r} , in direction \mathbf{u} and at frequency ω . More precisely, it can be shown from first principles that it is given by the Wigner transform of the field. In our context (scatterer displacements), it reads

$$\begin{aligned} \delta(k - k_0) \tilde{I}(\mathbf{r}, \mathbf{u}, \omega) &= \int \left\langle E\left(\mathbf{r} + \frac{\mathbf{s}}{2}, \omega\right) \tilde{E}^*\left(\mathbf{r} - \frac{\mathbf{s}}{2}, \omega\right) \right\rangle \\ &\quad \times e^{-i\mathbf{k}\mathbf{u}\cdot\mathbf{s}} d\mathbf{s}. \end{aligned} \quad (9)$$

Thus, solving for \tilde{I} gives direct access to the field-field correlation function \mathcal{C} . Equation (8) is very similar to the standard radiative transfer equation (RTE) [43], except that it includes an additional function $g(\mathbf{r}, \mathbf{u}, \mathbf{u}', \omega)$ that represents the decorrelation of the field at each scattering event due to the motion of scatterers. It is given by

$$g(\mathbf{r}, \mathbf{u}, \mathbf{u}', \omega) = \int e^{-ik_0(\mathbf{u}-\mathbf{u}')\cdot\Delta} f(\mathbf{r}, \Delta) d\Delta, \quad (10)$$

where \mathbf{u} and \mathbf{u}' are unit vectors representing the scattered and incoming directions for a given scattering process. $f(\mathbf{r}, \Delta)$ is the probability density of having a displacement Δ of a scatterer at the position \mathbf{r} . The position dependence is required since this displacement is induced by the radiation pressure, which can be heterogeneous inside the medium (in particular, at small depths). Equation (10) can be interpreted as follows: the decorrelation is due to the phase shift (Doppler shift) averaged over all accessible displacements for a scatterer. As a simple model, we consider that the amplitude of the displacement is proportional to the specific intensity, which leads to

$$\begin{aligned} f(\mathbf{r}, \Delta) &= \delta\left[\Delta - \beta I\left(\mathbf{r}, \frac{\Delta}{\Delta}, \omega\right)\right] \\ &\quad \times \left[\beta^2 \int I(\mathbf{r}, \mathbf{u}, \omega)^2 d\mathbf{u}\right]^{-1}, \end{aligned} \quad (11)$$

where β is a factor taking into account the link between the displacement and the value of the specific intensity. In the following, β is considered as a scaling parameter. In Eq. (11), $I(\mathbf{r}, \mathbf{u}, \omega)$ is the specific intensity without any displacements. Finally, $p(\mathbf{u}, \mathbf{u}', \omega)$ is the phase function representing the part of the energy incident from direction

\mathbf{u}' and scattered into direction \mathbf{u} . For the Gaussian disorder considered here, it is given by

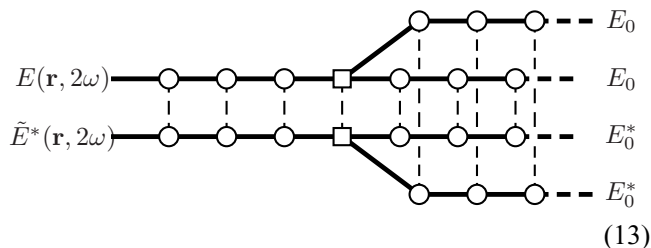
$$p(\mathbf{u}, \mathbf{u}', \omega) \propto p(k_0|\mathbf{u} - \mathbf{u}'|),$$

$$\text{where } p(q) = \exp\left[-\frac{q^2\ell^2}{2}\right], \quad (12)$$

and normalized such that $\int p(\mathbf{u}, \mathbf{u}', \omega)d\mathbf{u}' = 1$. Equation (8) can easily be interpreted using a random-walk approach. Indeed, light undergoes a random-walk the average step of which is given by the scattering mean free path $\ell_s(\omega)$ and the angular distribution of which at each scattering event is given by the phase function $p(\mathbf{u}, \mathbf{u}', \omega)$. A phase shift is introduced between the fields at each scattering event due to the displacement of the scatterers as described by the function $g(\mathbf{r}, \mathbf{u}, \mathbf{u}', \omega)$.

C. Second-harmonic regime

We now address the question of the generation and propagation of the second-harmonic light. As is usually done in homogeneous materials, we use a perturbative approach in order to compute the field at 2ω from the field at ω . The full process can be broken down into three steps. First, the linear field at ω propagates inside the material. Second, it is converted to a second harmonic on an arbitrary scatterer. Finally, this process is followed by the propagation of the second-harmonic field. The same sequence of processes also applies to the complex conjugate of the field. From this sequence, the most important point here is still the identification of the leading diagram, taking into account the nonlinearity. It is given by



where the squares represent the second-harmonic generation process. We could assume that the nonlinear processes for E and \tilde{E}^* occur at two positions with an arbitrary distance between them. However, this would lead to the propagation of the correlations $\langle E(\mathbf{r}, \omega)\tilde{E}^*(\mathbf{r}, 2\omega) \rangle$ or $\langle E(\mathbf{r}, 2\omega)\tilde{E}^*(\mathbf{r}, \omega) \rangle$, which are supposed to vanish since they involve fields at two different frequencies. The generations of the second-harmonic sources for E and \tilde{E}^* are then confined in a small volume with typical size ℓ . The relevance of the dominant diagram responsible for the second-harmonic correlation has to be carefully checked. For that purpose, we perform *ab initio* numerical simulations that are presented in Appendix C. Finally, the

diagram of Eq. (13) can be interpreted the following way: the right part represents the propagation of two specific intensities at frequency ω obeying Eq. (8) and the left part represents the propagation of the specific intensity at frequency 2ω . It is given by the following nonlinear RTE:

$$\left[\mathbf{u} \cdot \nabla_{\mathbf{r}} + \frac{1}{\ell_s(2\omega)}\right]\tilde{I}(\mathbf{r}, \mathbf{u}, 2\omega)$$

$$= \frac{1}{\ell_s(2\omega)} \int p(\mathbf{u}, \mathbf{u}', 2\omega)g(\mathbf{r}, \mathbf{u}, \mathbf{u}', 2\omega)\tilde{I}(\mathbf{r}, \mathbf{u}', 2\omega)d\mathbf{u}'$$

$$+ \alpha \iint p_{\text{SHG}}(\mathbf{u}, \mathbf{u}', \mathbf{u}'', \omega)g_{\text{SHG}}(\mathbf{r}, \mathbf{u}, \mathbf{u}', \mathbf{u}'', \omega)$$

$$\times \tilde{I}(\mathbf{r}, \mathbf{u}', \omega)\tilde{I}(\mathbf{r}, \mathbf{u}'', \omega)d\mathbf{u}'d\mathbf{u}''.$$
 (14)

This equation is the main theoretical result of this work. It shows that the second-harmonic specific intensity follows a similar transport equation as the fundamental intensity [Eq. (8)] but with a source term describing the nonlinear conversion process. Its physical interpretation is very simple. Light propagates first at frequency ω , which is described by the specific intensity $\tilde{I}(\mathbf{r}, \mathbf{u}'', \omega)$ solution to Eq. (8). Then, an SHG process occurs, which creates a source at frequency 2ω , the amplitude of which is given by the product of two specific intensities at ω . Finally, propagation at 2ω is described by the specific intensity $\tilde{I}(\mathbf{r}, \mathbf{u}', 2\omega)$, which follows Eq. (14). In this expression, α is a factor that takes into account all constants involved in the SHG process such as $\chi^{(2)}$. $p_{\text{SHG}}(\mathbf{u}, \mathbf{u}', \mathbf{u}'', \omega)$ is the SHG phase function. It involves three unit vectors. \mathbf{u}' and \mathbf{u}'' correspond to the incoming directions of the two specific intensities at ω and \mathbf{u} is the outgoing direction of the specific intensity at 2ω . In the case of the correlated disorder that we consider here, we have

$$p_{\text{SHG}}(\mathbf{u}, \mathbf{u}', \mathbf{u}'', \omega) \propto p(k_0|2\mathbf{u} - \mathbf{u}' - \mathbf{u}''|), \quad (15)$$

with $\int p_{\text{SHG}}(\mathbf{u}, \mathbf{u}', \mathbf{u}'', \omega)d\mathbf{u}'d\mathbf{u}'' = 1$. \mathbf{u} appears with a factor of 2 since it corresponds to the nonlinear specific intensity direction. $g_{\text{SHG}}(\mathbf{r}, \mathbf{u}, \mathbf{u}', \mathbf{u}'', \omega)$ is the decorrelation function, given by

$$g_{\text{SHG}}(\mathbf{r}, \mathbf{u}, \mathbf{u}', \mathbf{u}'', \omega) = \int e^{-ik_0(2\mathbf{u} - \mathbf{u}' - \mathbf{u}'') \cdot \Delta} f(\mathbf{r}, \Delta)d\Delta.$$
 (16)

It still corresponds to the decorrelation induced by a Doppler shift involving three beams, i.e., two incoming beams at frequency ω in directions \mathbf{u}' and \mathbf{u}'' and one outgoing beam at frequency 2ω in direction \mathbf{u} .

D. Numerical simulations

In order to solve the system of Eqs. (8) and (14), we develop a Monte Carlo scheme, which can be seen as

a random-walk process inside the material [44]. Three Monte Carlo simulations are performed in a slab geometry of thickness L under plane-wave illumination at normal incidence. The first is used to compute $I(\mathbf{r}, \mathbf{u}, \omega)$, the specific intensity in the absence of displacement of the scatterers. This is required in order to compute the probability density $f(\mathbf{r}, \mathbf{\Delta})$ to have a displacement $\mathbf{\Delta}$ at position \mathbf{r} . The second Monte Carlo simulation is used to compute $\tilde{I}(\mathbf{r}, \mathbf{u}, \omega)$, the specific intensity associated with the correlation function at ω . Finally, a last simulation is performed in order to compute $\tilde{I}(\mathbf{r}, \mathbf{u}, 2\omega)$, the specific intensity associated with the correlation function at 2ω . More precisely, the correlation functions are computed from the energy density at the output interface in transmission, i.e.,

$$C(\omega) = \frac{\int \tilde{I}(z=L, \mathbf{u}, \omega) d\mathbf{u}}{\int I(z=L, \mathbf{u}, \omega) d\mathbf{u}}, \quad (17)$$

$$C(2\omega) = \frac{\int \tilde{I}(z=L, \mathbf{u}, 2\omega) d\mathbf{u}}{\int I(z=L, \mathbf{u}, 2\omega) d\mathbf{u}}. \quad (18)$$

These computations are performed for different incident intensities I_0 (or different incident powers $\langle P \rangle$), meaning different probability densities $f(\mathbf{r}, \mathbf{\Delta})$, which correspond to different radiation pressures. Regarding the numerical parameters, it is important to keep in mind that the KDP powder used in the experiment has crystal grains of different sizes, ranging from $2 \mu\text{m}$ to $8 \mu\text{m}$. This makes the choice of the correlation length ℓ difficult. However, we test several values, showing that this is not a crucial parameter. Since the particles are large compared to the wavelength, we choose $k_0\ell = 3$ for the results presented in Fig. 4. This gives the anisotropy factors $g(\omega) = 0.89$ and $g(2\omega) = 0.97$. The thickness of the medium L as well as the transport mean free paths $\ell_t = \ell_s/(1-g)$ take the values measured experimentally, which gives $k_0L = 3012$ (for $L = 510 \mu\text{m}$), $k_0L = 4016$ (for $L = 680 \mu\text{m}$), $k_0\ell_t(\omega) = 2079$ and $k_0\ell_t(2\omega) = 998$. This finally leads to the normalized scattering mean free paths $k_0\ell_s(\omega) = 229$ and $k_0\ell_s(2\omega) = 30$.

We can observe that the results shown in Fig. 3 are reproduced qualitatively. The second-harmonic beam decorrelates faster than that of the fundamental frequency. The slopes of the decorrelation curves also reproduce the same trends seen in experiments, for the most part of the input-power range. The IR light shows a reducing slope followed by a rise at a certain pump power, while the frequency-doubled light shows a steady rise followed by a saturation region. Barring a minor difference at low powers, the experimental data exhibit the same behavior. The crossing of the two slope curves also happens at a lower pump power in the thicker sample, as seen in the experiments. The agreement with the experiments is very clear qualitatively but is not quantitative. The main reason should probably be investigated in relation to the

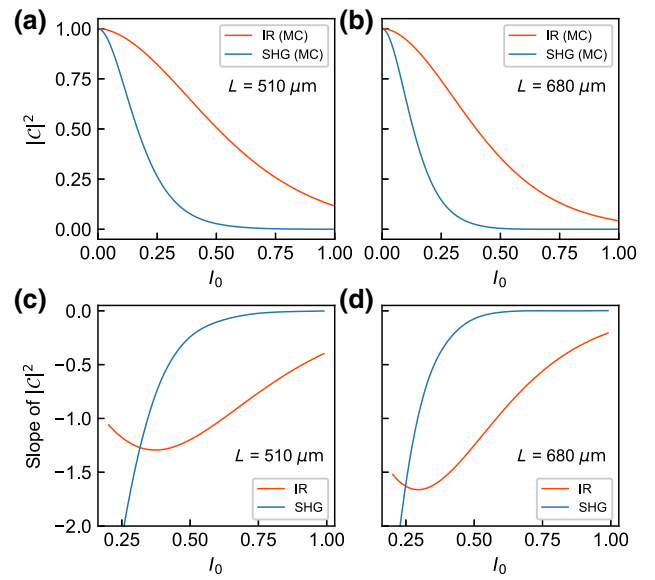


FIG. 4. (a),(b) Monte Carlo (MC) simulated correlation functions $|C|^2$ for the linear (red solid line) and second-harmonic (blue solid line) beams as a function of the incident intensity I_0 in arbitrary units: (a) $L = 510 \mu\text{m}$; (b) $L = 680 \mu\text{m}$. The range of I_0 is chosen such that the extreme values of the linear correlation $|C(\omega)|^2$ are in agreement with the experimental values $C_{\text{expe}}(\omega)$ presented. (c),(d) Slopes of $|C(\omega)|^2$ and $|C(2\omega)|^2$ calculated on each power value for the two samples: (c) $L = 510 \mu\text{m}$; (d) $L = 680 \mu\text{m}$. A qualitative agreement is immediately seen with the experimental behavior in Fig. 3.

dependence of the probability density f on the specific intensity I . Building this relationship is not a trivial task and is beyond the scope of the present work. A second potential effect, which has been neglected so far, is the role of the refractive index mismatch at the interfaces of the slab. In the Monte Carlo simulation, we verify that this does not substantially change the results up to a refractive index $n = 2$.

The faster decorrelation of the second-harmonic speckle can be explained through two different mechanisms. The first one corresponds to the decorrelation when the second-harmonic light is generated, which is represented by $g_{\text{SHG}}(\mathbf{r}, \mathbf{u}, \mathbf{u}', \mathbf{u}'', \omega)$. Its dependence on the three different directions through the relation $2\mathbf{u} - \mathbf{u}' - \mathbf{u}''$ favors a faster decorrelation. The second mechanism is due to the propagation of the second-harmonic field. The factor of 2 in $g(\mathbf{r}, \mathbf{u}, \mathbf{u}', 2\omega)$ also makes the correlation vanish faster than for the linear beam. For a small optical thickness, both effects play a role and have to be taken into account properly. This comes from the fact that photons experience few scattering events before escaping the medium and thus the decorrelations due to g_{SHG} and to g are of the same order of magnitude. On the other hand, for large optical thicknesses, many scattering events are involved and the contribution of g_{SHG} is negligible compared to that of g . Figure 5 illustrates this statement using the Monte Carlo

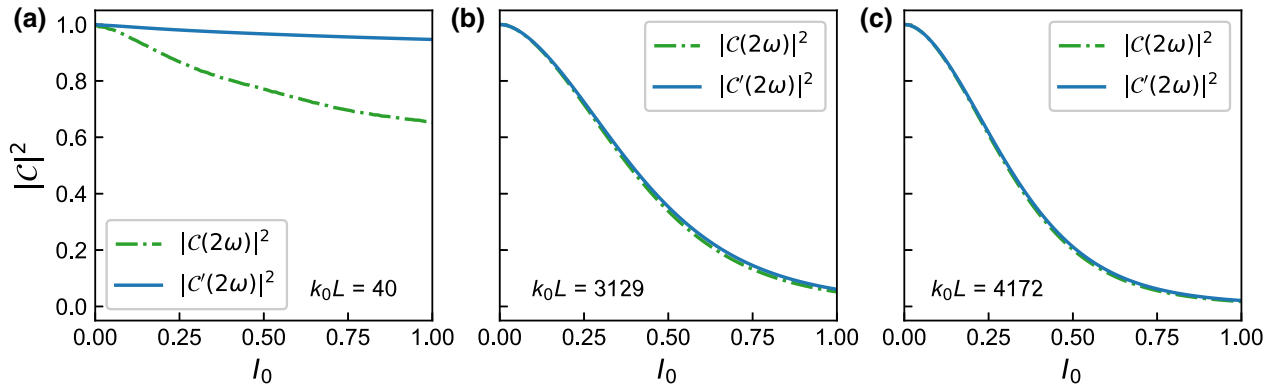


FIG. 5. Monte Carlo (MC) simulated correlation functions $|C|^2$ for the second-harmonic speckles taking into account all decorrelation effects (i.e., the effect of g and g_{SHG} , green dashed line) and only the decorrelation occurring during beam propagation (i.e., the effect of g , blue solid line). The computations are performed for (a) $k_0L = 40$, (b) $k_0L = 3129$, and (c) $k_0L = 4172$. The other parameters are the same as in Fig. 4.

simulations. This simple conclusion is also easily observed in the more simple case of statistically homogeneous and isotropic displacements discussed in Sec. III E.

E. Statistically homogeneous and isotropic displacements

Beyond the effect of radiation pressure that is examined in this study, it is also interesting to consider a displace-

ment probability for the scatterers that is homogeneous and isotropic, i.e., $f(\mathbf{r}, \Delta) = f(\Delta)/(4\pi\Delta^2)$. Indeed, considering large medium thicknesses compared to the transport mean free paths, i.e., $L \gg \{\ell_t(\omega), \ell_t(2\omega)\}$, we can derive diffusion equations for the linear and second-harmonic correlation functions. The derivation is detailed in Appendix D and leads to analytical expressions given by

$$C(\omega) = \frac{\kappa(\omega)L}{\sinh[\kappa(\omega)L]}, \quad (19)$$

$$C(2\omega) = \frac{6\mathcal{D}(\omega)}{\kappa(2\omega)L \sinh[\kappa(\omega)L]^2 \sinh[\kappa(2\omega)L]} \frac{\kappa(2\omega)^2 \{1 - \cosh[2\kappa(\omega)L]\} - 4\kappa(\omega)^2 \{1 - \cosh[\kappa(2\omega)L]\}}{\kappa(2\omega)^2 - 4\kappa(\omega)^2}, \quad (20)$$

where

$$\kappa = \sqrt{\frac{3}{\tilde{\ell}_t \tilde{\ell}_a}}, \quad \tilde{\ell}_t = \frac{\ell_s}{1 - \tilde{g}}, \quad (21)$$

$$\frac{1}{\tilde{\ell}_a} = \frac{1}{\ell_s} \left[1 - \int p(\mathbf{u}, \mathbf{u}') g(\mathbf{u}, \mathbf{u}') d\mathbf{u}' \right], \quad (22)$$

and

$$\tilde{g} = \frac{\int p(\mathbf{u}, \mathbf{u}') g(\mathbf{u}, \mathbf{u}') \mathbf{u} \cdot \mathbf{u}' d\mathbf{u}'}{\int p(\mathbf{u}, \mathbf{u}') g(\mathbf{u}, \mathbf{u}') d\mathbf{u}'}, \quad (23)$$

all these four quantities being defined at ω and 2ω . We also have

$$\mathcal{D}(\omega) = \frac{1}{4\pi} \int p_{\text{SHG}}(\mathbf{u}, \mathbf{u}', \mathbf{u}'', \omega) \times g_{\text{SHG}}(\mathbf{u}, \mathbf{u}', \mathbf{u}'', \omega) d\mathbf{u} d\mathbf{u}' d\mathbf{u}''. \quad (24) \quad \text{and}$$

We can clearly see from these expressions that the effect of the decorrelation during the propagation of the waves at ω or at 2ω can be seen as an absorption effect and is encoded in the κ functions. The decorrelation process taking place during the generation of the second-harmonic light is encoded in the \mathcal{D} function. Finally, these analytical expressions can be simplified in the even more particular case of isotropic scattering such that $p(\mathbf{u}, \mathbf{u}') = 1/(4\pi)$ and $p_{\text{SHG}}(\mathbf{u}, \mathbf{u}', \mathbf{u}'', \omega) = 1/(16\pi^2)$ and of a constant displacement amplitude d such that $k_0d \ll 1$ and $f(\Delta) = \delta(\Delta - d)$. This gives

$$\kappa(\omega)L = b(\omega)k_0d, \quad \kappa(2\omega)L = 2b(2\omega)k_0d, \quad (25)$$

$$\mathcal{D}(\omega) = \frac{1}{8\pi} \int_{\phi=0}^{2\pi} \int_{\mu=-1}^1 \int_{\mu'=-1}^1 \text{sinc} \left[k_0 d \sqrt{6 - 4\mu - 4\mu' + 2\mu\mu' + 2\sqrt{1 - \mu^2}\sqrt{1 - \mu'^2} \cos \phi} \right] d\mu d\mu' d\phi, \quad (26)$$

where $b = L/\ell_s$ is the optical thickness. These last expressions are very useful to gain further insights into the decorrelation effects encoded in functions $\kappa(\omega)$, $\kappa(2\omega)$, and $\mathcal{D}(\omega)$. In particular, as already noted in the numerical simulations, we clearly see that the decorrelation during propagation is stronger when the optical thicknesses $b(\omega)$ and $b(2\omega)$ increase, which reduces the effect of $\mathcal{D}(\omega)$. In the diffusive regime considered here, $\mathcal{D}(\omega)$ can thus be replaced by its limit when $k_0 d \rightarrow 0$, i.e., $\mathcal{D}(\omega) \sim 1$.

IV. DISCUSSION AND CONCLUSIONS

In summary, we experimentally investigate the decorrelation of speckle patterns with increasing pump power in a second-order nonlinear disordered medium. Simultaneous speckle measurements at the fundamental and second-harmonic wavelengths reveal a varying rate of decorrelation under the same incident power. The decorrelation arises from the microscopic displacements in the disorder configuration induced by the radiation pressure produced by the pump beam. In addition, the second-harmonic correlation decreases faster than the fundamental. We lay the foundations of a theoretical model that describes the synergy of second-order nonlinearity and light diffusion. The model demarcates the contribution of two components in the decorrelation, namely, one arising from the generation of second-harmonic light and the other arising from the propagation thereof. For the samples and input powers employed in our experiments, the former seems to be the stronger contributor. Wider investigations of the model show that the relative strengths of the two components depend upon the degree of disorder. With regard to the differences in the experimental and computed results, we discuss the origins qualitatively as follows. The actual displacement at a location \mathbf{r} is dependent on the specific intensity at that location and the size and shape of the particle at that location. This is too intricate a parameter to calculate and we do not venture to do so. In the theory, the sample is homogeneously disordered and particle size is not a parameter in computing the displacement under radiation pressure. At a future stage, a distribution in the displacements may be invoked in the theory. We believe that these unavoidable differences in the experimental samples and theoretical assumptions limit the agreement in the respective results. This study sheds light on the subtle mechanism of nonlinear conversion in disordered media, with expected outcomes in fundamental studies in mesoscopic wave transport, as well as the design of efficient materials for nonlinear generation of light.

ACKNOWLEDGMENTS

R.S. and S.M. acknowledge the support from Sandip Mondal and N. Sreeman Kumar during the experiment. We are all grateful to the Department of Atomic Energy (DAE), Government of India for funding for Project Identification No. RTI4002 under the DAE OM No. 1303/1/2020/R&D-II/DAE/5567, dated August 20, 2020; and from the Swarnajayanti Fellowship, Department of Science and Technology, Ministry of Science and Technology, India. This work has also received support under the program “Investissements d’Avenir,” launched by the French government. The authors declare no conflicts of interest.

APPENDIX A: A DIFFERENT EXPERIMENT TO VALIDATE PARTICLE MOVEMENT DUE TO LASER RADIATION PRESSURE

We carry out experiments to demonstrate that the scatterer displacements are due to radiation pressure. Specifically, a stabilized frequency, low-power cw laser (He:Ne, $\lambda = 632.8$ nm) is made incident onto the sample simultaneously with the pump. The phase stability of the He:Ne laser is confirmed by performing a simple experiment. First, we focus the He:Ne laser on a ground-glass diffuser and subsequently capture the transmitted speckle pattern on a CMOS camera over 30 min at 1-min intervals. In Fig. 6, we plot the speckle correlation calculated with respect to the initial speckle pattern. We observe that the correlation coefficient always stays close to the ideal value of 1 (indicated by the red dashed line), which proves that our He:Ne laser is highly stable.

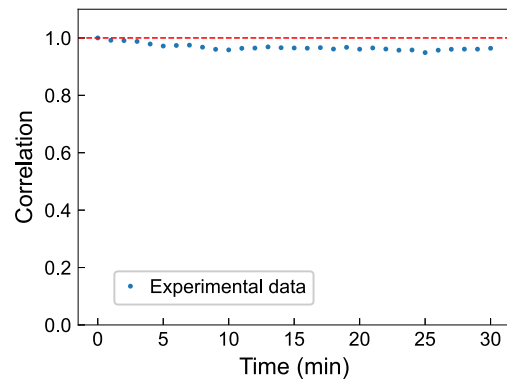


FIG. 6. The speckle correlation, showing the high stability of the He:Ne laser.

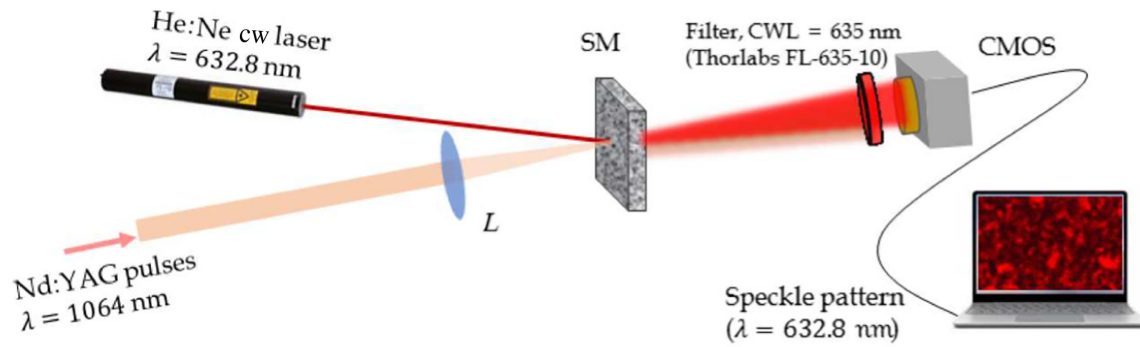


FIG. 7. The experimental setup to investigate the movements of the particles due to a high input-laser power: L, lens; SM, scattering medium; CML, central wavelength.

It is well known that the speckle pattern produced by a scattering medium remains static if the scatterers of the medium do not move. A schematic of the experimental setup is depicted in Fig. 7. Nd:YAG laser pulses (pulse width 35 ps, repetition rate 1 Hz) with a fundamental wavelength of 1064 nm are falling normally on the sample. A cw phase-stabilized He:Ne laser with a wavelength of 632.8 nm is also made incident on the sample at the same position. Here, it should be noted that the sample behaves as a linear medium for the laser coming from the He:Ne, whereas Nd:YAG pulses, at a sufficient input power, can generate nonlinear photons. As a result, in transmission, we can retrieve three speckle patterns, namely, red ($\lambda = 632.8$ nm), IR ($\lambda = 1064$ nm), and SHG ($\lambda = 532$ nm). For the current purpose, the speckle dynamics of the red light is monitored. A laser line filter (Thorlabs, FL-635-10) with a center wavelength of 635 nm is placed in front of a CMOS camera (Thorlabs). We capture the speckle patterns of red light while increasing the Nd:YAG laser power from very low to high and again from high to low. The speckles are reported in Figs. 8(a)–8(f).

The first two images [Figs. 8(a) and 8(b)] correspond to consecutive Nd:YAG laser shots where the input power is very low. Clearly, the speckle patterns are almost the same over these shots. Next, we increase the input power of the Nd:YAG laser such that the second harmonic is efficiently generated. Figures 8(c) and 8(d) are consecutive speckle images corresponding to this input power and they are seen to be obviously different. This shows that the configuration of the sample is changing from shot to shot at high power. Next, we again decrease the Nd:YAG power to the minimum power and grab Figs. 8(e) and 8(f) on consecutive laser pulses. Again, the speckle becomes stable when the input power reaches a very low value, since the sample is stable. Further, it is also observed that the initial [Figs. 8(a) and 8(b)] and final [Figs. 8(e) and 8(f)] red speckle patterns, although at the same low power, are completely different, which indicates that the particle configuration inside the sample has changed over the experiment. All of this clearly indicates the scatterer displacements due to the high input power.

This experiment allows us to rule out thermal effects. Thermal effects tend to work on longer time scales than

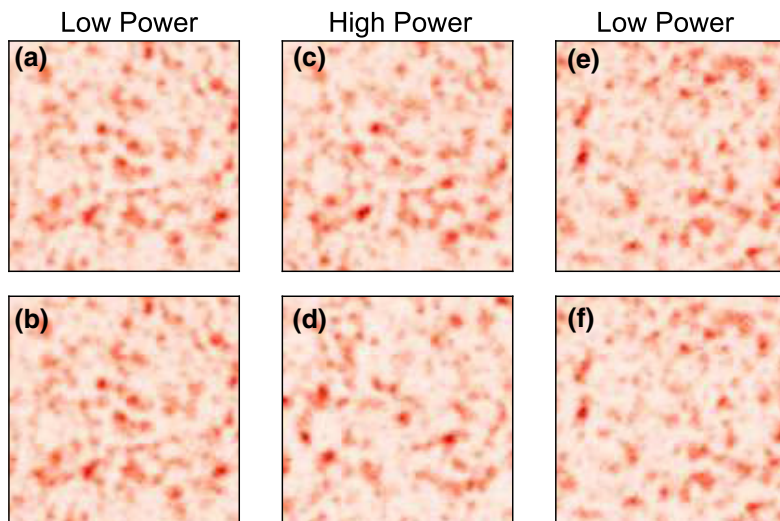


FIG. 8. The speckle patterns of red light in different scenarios. (a),(b) The beginning of the experiment, with a low power of the input pulsed laser. (c),(d) The high power of the input pulsed laser. (e),(f) The ending of the experiment, with a low power of the input pulsed laser.

impact by the radiation pressure. In the speckle pattern generated by the He:Ne laser, we observe that the speckle is instantaneously reorganized when the pulse hits the sample and that immediately thereafter, the pattern is stable. There is no gradual and continuous change in the speckle for a finite time after the pulse. This motivates us to assert that, although thermal effects cannot be ruled out completely, the major contribution to the decorrelation arises from displacement due to pulse impact. Furthermore, the laser pulses are shot at too low a repetition rate to expect a cumulative thermal effect.

APPENDIX B: TRANSPORT-MODEL DERIVATION

This appendix is devoted to the derivation of the transport model used to estimate the correlation function C in the linear as well as in the second-harmonic regime. This derivation is largely inspired by the standard multiple-scattering theory, details of which can be found in several references (see, e.g., Refs. [42,45,46]). The generalization presented here allows us to take into account (1) scatterer displacements and (2) second-harmonic generation. Regarding the first point, the reader can also refer to Ref. [40], which presents a similar derivation. Regarding the second point, a similar approach has been used in the context of photon echoes, described in Ref. [47].

1. Disorder model and scattering potential

We consider a continuous disorder model described by a fluctuating permittivity $\epsilon(\mathbf{r}, \omega)$ and a fluctuating second-order nonlinear susceptibility $\chi(\mathbf{r})$. We choose to characterize their statistical properties by a Gaussian correlation function that is identical for both ϵ and χ , since the disorder at the origin of the scattering and of second-harmonic generation is the same. This gives

$$C_\epsilon(\mathbf{r}, \mathbf{r}', \omega) = \langle \delta\epsilon(\mathbf{r}, \omega) \delta\epsilon(\mathbf{r}', \omega) \rangle = |\Delta\epsilon(\omega)|^2 C(|\mathbf{r} - \mathbf{r}'|), \quad (\text{B1})$$

$$C_\chi(\mathbf{r}, \mathbf{r}') = \langle \delta\chi(\mathbf{r}) \delta\chi(\mathbf{r}') \rangle = |\Delta\chi|^2 C(|\mathbf{r} - \mathbf{r}'|), \quad (\text{B2})$$

with

$$C(|\mathbf{r} - \mathbf{r}'|) = \exp\left[-\frac{|\mathbf{r} - \mathbf{r}'|^2}{2\ell^2}\right], \quad (\text{B3})$$

and where $|\Delta\epsilon(\omega)|^2$ and $|\Delta\chi|^2$ are the amplitudes and ℓ is the correlation length. $\delta\epsilon(\mathbf{r}, \omega) = \epsilon(\mathbf{r}, \omega) - \langle \epsilon(\omega) \rangle$ is the fluctuating part of the permittivity. Similarly, $\delta\chi(\mathbf{r}) = \chi(\mathbf{r}) - \langle \chi \rangle$ is the fluctuating part of the second-order susceptibility. The disorder correlation function depends only on $|\mathbf{r} - \mathbf{r}'|$ because we consider that the disorder is statistically isotropic and homogeneous. From this model, we

first define the scattering potential, which is at the root of the multiple-scattering theory. It is given by

$$V(\mathbf{r}, \omega) = k_0^2 [\epsilon(\mathbf{r}, \omega) - \epsilon_b(\omega)]. \quad (\text{B4})$$

ϵ_b is the background permittivity corresponding to the reference nonscattering medium. It is thus homogeneous. We now consider that there are scatterer displacements, for example, under the action of the radiation pressure but this can be a completely different physical process. After displacements, the new potential is given by

$$\tilde{V}(\mathbf{r}, \omega) = V(\mathbf{r} - \mathbf{\Delta}(\mathbf{r}), \omega), \quad (\text{B5})$$

where $\mathbf{\Delta}(\mathbf{r})$ is the displacement at position \mathbf{r} . In the following, we consider that this displacement is constant over a length scale of the order of ℓ . This allows us to take the Fourier transform of Eq. (B5) considering no position dependence in $\mathbf{\Delta}$, which gives

$$\tilde{V}(\mathbf{k}, \omega) = V(\mathbf{k}, \omega) \exp[-i\mathbf{k} \cdot \mathbf{\Delta}(\mathbf{r})]. \quad (\text{B6})$$

In a similar way, we have

$$\tilde{\chi}(\mathbf{r}) = \chi(\mathbf{r} - \mathbf{\Delta}(\mathbf{r})), \quad (\text{B7})$$

which leads to

$$\tilde{\chi}(\mathbf{k}) = \chi(\mathbf{k}) \exp[-i\mathbf{k} \cdot \mathbf{\Delta}(\mathbf{r})]. \quad (\text{B8})$$

2. Self-energy and intensity vertex

We now focus on the computation of some important building blocks regarding wave propagation in complex media, which are the self-energy Σ and the intensity vertex Γ . Similarly to the scattering potential, we show how their expressions are modified in order to take the scatterer displacements into account.

We first consider the self-energy Σ and, more importantly, its counterpart denoted by $\tilde{\Sigma}$ when scatterer displacements are present. The self-energy is an important quantity entering the Dyson equation that drives the evolution of the statistical average electric field propagating inside a strongly scattering medium. It contains all possible scattering sequences that cannot be statistically factorized. In a dilute medium where the scattering mean free path is large compared to the wavelength, it can be limited to the first two orders and written as

$$\Sigma(\mathbf{r}, \mathbf{r}', \omega) = \langle V(\mathbf{r}, \omega) \rangle \delta(\mathbf{r} - \mathbf{r}') + \langle V(\mathbf{r}, \omega) G_b(\mathbf{r} - \mathbf{r}', \omega) V(\mathbf{r}', \omega) \rangle_c, \quad (\text{B9})$$

where $\langle \cdot \rangle_c$ represents a statistical average restricted to the connected part, i.e., $\langle VG_bV \rangle_c = \langle VG_bV \rangle - \langle V \rangle G_b \langle V \rangle$. G_b is the Green function in the reference medium, which

describes the field propagation between two consecutive scattering events on the potential V . For the case of scatterer displacements, we have

$$\begin{aligned} \tilde{\Sigma}(\mathbf{r}, \mathbf{r}', \omega) &= \langle \tilde{V}(\mathbf{r}, \omega) \rangle \delta(\mathbf{r} - \mathbf{r}') \\ &+ \langle \tilde{V}(\mathbf{r}, \omega) G_b(\mathbf{r} - \mathbf{r}', \omega) \tilde{V}(\mathbf{r}', \omega) \rangle_c. \end{aligned} \quad (\text{B10})$$

It is important to keep in mind that the statistical average performed here is not only an average over all possible configurations of the disorder but is also an average over the displacements. By Fourier transforming Eqs. (B10) and (B9) and using Eq. (B6), we obtain

$$\begin{aligned} \tilde{\Sigma}(\mathbf{k}, \mathbf{k}', \omega) &= \Sigma(\mathbf{k}, \mathbf{k}', \omega) \int \exp[-i(\mathbf{k} - \mathbf{k}') \cdot \mathbf{\Delta}] \\ &\times f(\mathbf{r}, \mathbf{\Delta}) d\mathbf{\Delta}, \end{aligned} \quad (\text{B11})$$

where $f(\mathbf{r}, \mathbf{\Delta})$ is the probability density of having a displacement $\mathbf{\Delta}$ at position \mathbf{r} . From the statistical homogeneity and isotropy of the disorder, we obtain

$$\begin{aligned} \Sigma(\mathbf{k}, \mathbf{k}', \omega) &= 8\pi^3 \delta(\mathbf{k} - \mathbf{k}') \check{\Sigma}(k, \omega) \quad \text{and} \\ \check{\Sigma}(\mathbf{k}, \mathbf{k}', \omega) &= 8\pi^3 \delta(\mathbf{k} - \mathbf{k}') \check{\check{\Sigma}}(k, \omega), \end{aligned} \quad (\text{B12})$$

which leads to

$$\check{\check{\Sigma}}(k, \omega) = \check{\Sigma}(k, \omega), \quad (\text{B13})$$

where $\check{\Sigma}$ and $\check{\check{\Sigma}}$ are the reduced self-energies. Since the extinction mean free path is given by the imaginary part of the reduced self-energy, we have

$$\frac{1}{\ell_e(\omega)} = \frac{\text{Im} \check{\Sigma}(k_0, \omega)}{k_0} = \frac{\text{Im} \check{\check{\Sigma}}(k_0, \omega)}{k_0} = \frac{1}{\check{\ell}_e(\omega)}. \quad (\text{B14})$$

By invoking the nonabsorbing nature of the medium, we finally obtain equality between the scattering mean free paths with and without scatterer displacements. Insertion of the expression for the correlation function C_ϵ into Eq. (B9) leads to

$$\frac{1}{\check{\ell}_s(\omega)} = \frac{1}{\ell_s(\omega)} = \frac{k_0^4 |\Delta\epsilon(\omega)|^2}{16\pi^2} \int C(q) d\Omega, \quad (\text{B15})$$

where $q = 2k_0 \sin(\theta/2)$ is the modulus of the scattering vector and $d\Omega = \sin\theta d\theta d\phi$ is the elementary solid angle

in standard spherical units. From Eq. (B3), we obtain

$$\begin{aligned} C(q) &= \int \exp\left[-\frac{\mathbf{R}^2}{2\ell^2} - i\mathbf{q} \cdot \mathbf{R}\right] d\mathbf{R} \\ &= \ell^3 (2\pi)^{3/2} \exp\left[-\frac{q^2 \ell^2}{2}\right], \end{aligned} \quad (\text{B16})$$

which finally gives

$$\frac{1}{\check{\ell}_s(\omega)} = \frac{1}{\ell_s(\omega)} = k_0^2 \ell |\Delta\epsilon(\omega)|^2 \frac{\sqrt{2\pi}}{4} [1 - \exp(-2k_0^2 \ell^2)]. \quad (\text{B17})$$

The same analysis now has to be applied to the intensity vertex Γ and its counterpart $\check{\Gamma}$ when scatterer displacements are present. The intensity vertex is an important quantity entering the Bethe-Salpeter equation that describes the evolution of the field-field correlation function. It contains all possible scattering sequences for the field and its complex-conjugate counterpart that cannot be statistically factorized. Still, in a dilute medium, it can be limited to the first order and written as

$$\Gamma(\mathbf{r}, \mathbf{r}', \boldsymbol{\rho}, \boldsymbol{\rho}', \omega) = \langle V(\mathbf{r}, \omega) V^*(\boldsymbol{\rho}, \omega) \rangle_c \delta(\mathbf{r} - \mathbf{r}') \delta(\boldsymbol{\rho} - \boldsymbol{\rho}'). \quad (\text{B18})$$

For the case of scatterer displacements, we have

$$\check{\Gamma}(\mathbf{r}, \mathbf{r}', \boldsymbol{\rho}, \boldsymbol{\rho}', \omega) = \langle V(\mathbf{r}, \omega) \check{V}^*(\boldsymbol{\rho}, \omega) \rangle_c \delta(\mathbf{r} - \mathbf{r}') \delta(\boldsymbol{\rho} - \boldsymbol{\rho}'). \quad (\text{B19})$$

It is important to note that the correlation \mathcal{C} involves the electric field before any displacement (E) and its complex-conjugate counterpart after displacement (\check{E}^*). This is the reason why only the complex-conjugated potential is replaced in Eq. (B19) compared to Eq. (B18). We also note that although the potential is real, we keep the complex-conjugate notation for the sake of understanding, i.e., to show that it applies to the complex-conjugate field. By Fourier transforming Eqs. (B19) and (B18) and using Eqs. (B6), we obtain

$$\begin{aligned} \check{\Gamma}(\mathbf{k}, \mathbf{k}', \boldsymbol{\kappa}, \boldsymbol{\kappa}', \omega) &= \Gamma(\mathbf{k}, \mathbf{k}', \boldsymbol{\kappa}, \boldsymbol{\kappa}', \omega) \\ &\times \int \exp[-i(\boldsymbol{\kappa} - \boldsymbol{\kappa}') \cdot \mathbf{\Delta}] f(\mathbf{r}, \mathbf{\Delta}) d\mathbf{\Delta}. \end{aligned} \quad (\text{B20})$$

From the statistical homogeneity of the disorder, we obtain

$$\begin{aligned} \check{\check{\Gamma}}(\mathbf{k}, \mathbf{k}', \boldsymbol{\kappa}, \boldsymbol{\kappa}', \omega) &= 8\pi^3 \delta(\mathbf{k} - \mathbf{k}' - \boldsymbol{\kappa} + \boldsymbol{\kappa}') \\ &\times \Gamma(\mathbf{k}, \mathbf{k}', \boldsymbol{\kappa}, \boldsymbol{\kappa}', \omega), \end{aligned} \quad (\text{B21})$$

$$\begin{aligned} \check{\check{\Gamma}}(\mathbf{k}, \mathbf{k}', \boldsymbol{\kappa}, \boldsymbol{\kappa}', \omega) &= 8\pi^3 \delta(\mathbf{k} - \mathbf{k}' - \boldsymbol{\kappa} + \boldsymbol{\kappa}') \\ &\times \check{\check{\Gamma}}(\mathbf{k}, \mathbf{k}', \boldsymbol{\kappa}, \boldsymbol{\kappa}', \omega), \end{aligned} \quad (\text{B22})$$

which finally leads to

$$\begin{aligned} \check{\check{\Gamma}}(\mathbf{k}, \mathbf{k}', \boldsymbol{\kappa}, \boldsymbol{\kappa}', \omega) &= \check{\check{\Gamma}}(\mathbf{k}, \mathbf{k}', \boldsymbol{\kappa}, \boldsymbol{\kappa}', \omega) \\ &\times \int \exp[-i(\boldsymbol{\kappa} - \boldsymbol{\kappa}') \cdot \boldsymbol{\Delta}] f(\mathbf{r}, \boldsymbol{\Delta}) d\boldsymbol{\Delta}, \end{aligned} \quad (\text{B23})$$

where $\check{\check{\Gamma}}$ and $\check{\check{\Gamma}}$ are the reduced intensity vertices. The standard phase function is given by $\check{\check{\Gamma}}$ through the relation

$$\frac{1}{\ell_s(\omega)} p(\mathbf{u}, \mathbf{u}', \omega) = \frac{1}{16\pi^2} \check{\check{\Gamma}}(k_0 \mathbf{u}, k_0 \mathbf{u}', k_0 \mathbf{u}, k_0 \mathbf{u}', \omega). \quad (\text{B24})$$

By definition, the phase function p is normalized such that

$$\int p(\mathbf{u}, \mathbf{u}', \omega) d\mathbf{u}' = 1. \quad (\text{B25})$$

These results allow us to define a generalized phase function \tilde{p} for the case where there are scatterer displacements, given by

$$\begin{aligned} \frac{1}{\tilde{\ell}_s(\omega)} \tilde{p}(\mathbf{r}, \mathbf{u}, \mathbf{u}', \omega) &= \frac{1}{\ell_s(\omega)} p(\mathbf{u}, \mathbf{u}', \omega) g(\mathbf{r}, \mathbf{u}, \mathbf{u}', \omega) \\ &= \frac{1}{16\pi^2} \check{\check{\Gamma}}(k_0 \mathbf{u}, k_0 \mathbf{u}', k_0 \mathbf{u}, k_0 \mathbf{u}', \omega), \end{aligned} \quad (\text{B26})$$

where

$$g(\mathbf{r}, \mathbf{u}, \mathbf{u}', \omega) = \int \exp[-i\mathbf{q} \cdot \boldsymbol{\Delta}] f(\mathbf{r}, \boldsymbol{\Delta}) d\boldsymbol{\Delta}, \quad (\text{B27})$$

and $\mathbf{q} = k_0(\mathbf{u} - \mathbf{u}')$ is the scattering vector. Substitution of the expression of the correlation function C_ϵ into Eq. (B18) leads to

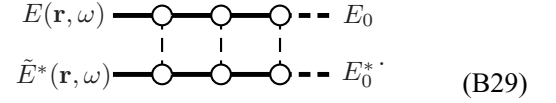
$$p(\mathbf{u}, \mathbf{u}', \omega) = \frac{k_0^2 \ell^2 \exp[-q^2 \ell^2 / 2]}{2\pi [1 - \exp(-2k_0^2 \ell^2)]}. \quad (\text{B28})$$

This concludes the computation of the building blocks required to describe light propagation in a diluted dynamic scattering medium.

3. Linear regime

We now consider the case of light transport in the linear regime. In a dilute medium such that $k_0 \ell_s \gg 1$, we can show that the field and its complex conjugate follow the

same scattering sequences (after statistical average), which can be represented by the following diagram:



In this representation, the top line represents a path for the electric field E and the bottom line is for a path of its complex conjugate \tilde{E}^* in the presence of scatterer displacements. The solid and dashed thick lines correspond to average Green functions (describing propagation between consecutive scattering events) and average fields, respectively. The circles denote scattering events and the vertical dashed lines represent statistical correlations between scattering events through Eq. (B1).

This specific diagram is called the ladder and is the leading contribution to the expression of the field-field correlation function C . Indeed, the fact that it corresponds to the same path for the field and its complex conjugate implies that there is always constructive interference between both. From this diagram, we deduce that the correlation function C is described by a RTE and can be written as [42]

$$\begin{aligned} \left[\mathbf{u} \cdot \nabla_{\mathbf{r}} + \frac{1}{\ell_s(\omega)} \right] \tilde{I}(\mathbf{r}, \mathbf{u}, \omega) \\ = \frac{1}{\ell_s(\omega)} \int p(\mathbf{u}, \mathbf{u}', \omega) g(\mathbf{r}, \mathbf{u}, \mathbf{u}', \omega) \tilde{I}(\mathbf{r}, \mathbf{u}', \omega) d\mathbf{u}', \end{aligned} \quad (\text{B30})$$

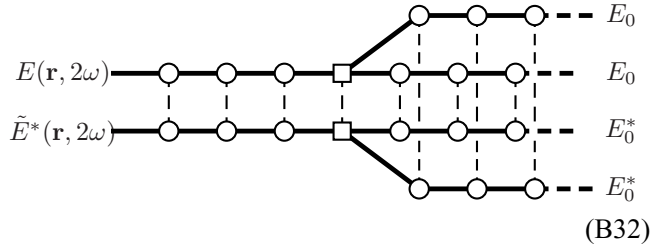
where the specific intensity \tilde{I} is defined by the field-field correlation

$$\begin{aligned} \delta(k - k_0) \tilde{I}(\mathbf{r}, \mathbf{u}, \omega) \\ = \int \left\langle E\left(\mathbf{r} + \frac{\mathbf{s}}{2}, \omega\right) \tilde{E}^*\left(\mathbf{r} - \frac{\mathbf{s}}{2}, \omega\right) \right\rangle e^{-i\mathbf{k} \cdot \mathbf{u} \cdot \mathbf{s}} d\mathbf{s}. \end{aligned} \quad (\text{B31})$$

4. Second-harmonic regime

We now move on to the second-harmonic regime. As stated in the main text, we apply a perturbative approach to compute the second-harmonic correlation. This means that we have first the propagation of the field at the frequency ω , then second-harmonic generation, and finally propagation of the field at the frequency 2ω . That being said, the most difficult task now is to determine the typical pairs of paths for the field and its complex conjugate that make the leading contribution to the correlation. This is equivalent to determining the diagrams that lead to constructive interference. We follow the same idea as for the linear regime, thus assuming that we have essentially ladder diagrams for the beams at ω and 2ω . However, these ladders have to be connected by a kernel corresponding to the second-harmonic

generation process. This leads to the diagram



where the squares denote the second-harmonic processes. We may consider that the nonlinear processes occur at two different positions for the electric field E and its complex-conjugate counterpart \tilde{E}^* . However, this would lead to propagation of the correlations $\langle E(\mathbf{r}, \omega)\tilde{E}^*(\mathbf{r}, 2\omega) \rangle$ or $\langle E(\mathbf{r}, 2\omega)\tilde{E}^*(\mathbf{r}, \omega) \rangle$, which are supposed to vanish since they involve fields at two different frequencies. This is the reason why we have a disorder correlation function C_ϵ between the second-harmonic processes (dashed line between the squares). Strictly speaking, we should also take into account the degeneracy of the diagram (factor 4). Indeed, it corresponds to all possible permutations of the incident fields. However, this does not play any role in the following and this factor is taken into account in the constant α .

The kernel dressed with the two ladders at frequency ω can be considered as a source term for the second-harmonic ladder. It is given by

$$\begin{aligned}
 S(\mathbf{r}, \boldsymbol{\rho}, 2\omega) &= \int \langle G(\mathbf{r} - \mathbf{r}', 2\omega) \rangle \langle G^*(\boldsymbol{\rho} - \boldsymbol{\rho}', 2\omega) \rangle \\
 &\quad \times \tilde{\Gamma}_{\text{SHG}}(\mathbf{r}', \mathbf{r}'', \mathbf{r}''', \boldsymbol{\rho}', \boldsymbol{\rho}'', \boldsymbol{\rho}''', 2\omega) \\
 &\quad \times \langle E(\mathbf{r}'', \omega)\tilde{E}^*(\boldsymbol{\rho}'', 2\omega) \rangle \\
 &\quad \times \langle E(\mathbf{r}''', \omega)\tilde{E}^*(\boldsymbol{\rho}''', 2\omega) \rangle \\
 &\quad \times d\mathbf{r}' d\mathbf{r}'' d\mathbf{r}''' d\boldsymbol{\rho}' d\boldsymbol{\rho}'' d\boldsymbol{\rho}''', \quad (\text{B33})
 \end{aligned}$$

where $\tilde{\Gamma}_{\text{SHG}}$ is the SHG vertex given by

$$\begin{aligned}
 \tilde{\Gamma}_{\text{SHG}}(\mathbf{r}, \mathbf{r}', \mathbf{r}'', \boldsymbol{\rho}, \boldsymbol{\rho}', \boldsymbol{\rho}'', \omega) &= \langle \chi(\mathbf{r})\tilde{\chi}^*(\boldsymbol{\rho}) \rangle_c \delta(\mathbf{r} - \mathbf{r}')\delta(\mathbf{r} - \mathbf{r}'')\delta(\boldsymbol{\rho} - \boldsymbol{\rho}')\delta(\boldsymbol{\rho} - \boldsymbol{\rho}''). \quad (\text{B34})
 \end{aligned}$$

Similarly to the case of $\tilde{\Gamma}$, we keep the complex-conjugate notation for the second-order susceptibility although it is a real quantity, in order to remind us that it corresponds to the complex-conjugate field. Without any scatterer displacement, we have

$$\begin{aligned}
 \Gamma_{\text{SHG}}(\mathbf{r}, \mathbf{r}', \mathbf{r}'', \boldsymbol{\rho}, \boldsymbol{\rho}', \boldsymbol{\rho}'', \omega) &= \langle \chi(\mathbf{r})\tilde{\chi}^*(\boldsymbol{\rho}) \rangle_c \delta(\mathbf{r} - \mathbf{r}')\delta(\mathbf{r} - \mathbf{r}'')\delta(\boldsymbol{\rho} - \boldsymbol{\rho}')\delta(\boldsymbol{\rho} - \boldsymbol{\rho}''). \quad (\text{B35})
 \end{aligned}$$

By Fourier transforming Eqs. (B34) and (B35) and making use of Eq. (B8), we obtain

$$\begin{aligned}
 \tilde{\Gamma}_{\text{SHG}}(\mathbf{k}, \mathbf{k}', \mathbf{k}'', \boldsymbol{\kappa}, \boldsymbol{\kappa}', \boldsymbol{\kappa}'', \omega) &= \Gamma_{\text{SHG}}(\mathbf{k}, \mathbf{k}', \mathbf{k}'', \boldsymbol{\kappa}, \boldsymbol{\kappa}', \boldsymbol{\kappa}'', \omega) \\
 &\quad \times \int \exp[-i(\boldsymbol{\kappa} - \boldsymbol{\kappa}' - \boldsymbol{\kappa}'') \cdot \boldsymbol{\Delta}] f(\mathbf{r}, \boldsymbol{\Delta}) d\boldsymbol{\Delta}. \quad (\text{B36})
 \end{aligned}$$

From the statistical homogeneity of the disorder, we obtain

$$\begin{aligned}
 \check{\Gamma}_{\text{SHG}}(\mathbf{k}, \mathbf{k}', \mathbf{k}'', \boldsymbol{\kappa}, \boldsymbol{\kappa}', \boldsymbol{\kappa}'', \omega) &= 8\pi^3 \delta(\mathbf{k} - \mathbf{k}' - \mathbf{k}'' - \boldsymbol{\kappa} + \boldsymbol{\kappa}' + \boldsymbol{\kappa}'') \\
 &\quad \times \Gamma_{\text{SHG}}(\mathbf{k}, \mathbf{k}', \mathbf{k}'', \boldsymbol{\kappa}, \boldsymbol{\kappa}', \boldsymbol{\kappa}'', \omega), \quad (\text{B37})
 \end{aligned}$$

$$\begin{aligned}
 \check{\check{\Gamma}}_{\text{SHG}}(\mathbf{k}, \mathbf{k}', \mathbf{k}'', \boldsymbol{\kappa}, \boldsymbol{\kappa}', \boldsymbol{\kappa}'', \omega) &= 8\pi^3 \delta(\mathbf{k} - \mathbf{k}' - \mathbf{k}'' - \boldsymbol{\kappa} + \boldsymbol{\kappa}' + \boldsymbol{\kappa}'') \\
 &\quad \times \tilde{\Gamma}_{\text{SHG}}(\mathbf{k}, \mathbf{k}', \mathbf{k}'', \boldsymbol{\kappa}, \boldsymbol{\kappa}', \boldsymbol{\kappa}'', \omega), \quad (\text{B38})
 \end{aligned}$$

which finally leads to

$$\begin{aligned}
 \check{\check{\Gamma}}_{\text{SHG}}(\mathbf{k}, \mathbf{k}', \mathbf{k}'', \boldsymbol{\kappa}, \boldsymbol{\kappa}', \boldsymbol{\kappa}'', \omega) &= \check{\check{\Gamma}}_{\text{SHG}}(\mathbf{k}, \mathbf{k}', \mathbf{k}'', \boldsymbol{\kappa}, \boldsymbol{\kappa}', \boldsymbol{\kappa}'', \omega) \\
 &\quad \times \int \exp[-i(\boldsymbol{\kappa} - \boldsymbol{\kappa}' - \boldsymbol{\kappa}'') \cdot \boldsymbol{\Delta}] f(\mathbf{r}, \boldsymbol{\Delta}) d\boldsymbol{\Delta}, \quad (\text{B39})
 \end{aligned}$$

where $\check{\check{\Gamma}}_{\text{SHG}}$ and $\check{\Gamma}_{\text{SHG}}$ are the reduced SHG vertices. From this, we can define a SHG phase function given by

$$\begin{aligned}
 \alpha p_{\text{SHG}}(\mathbf{u}, \mathbf{u}', \mathbf{u}'', \omega) &= \frac{1}{125\pi^5} \check{\check{\Gamma}}_{\text{SHG}}(2k_0\mathbf{u}, k_0\mathbf{u}', k_0\mathbf{u}'', 2k_0\mathbf{u}, k_0\mathbf{u}', k_0\mathbf{u}'', \omega). \quad (\text{B40})
 \end{aligned}$$

α is a coefficient that takes into account all constants involved in the second-harmonic process and is such that the second-harmonic phase function is normalized, i.e.,

$$\int p_{\text{SHG}}(\mathbf{u}, \mathbf{u}', \mathbf{u}'', \omega) d\mathbf{u}' d\mathbf{u}'' = 1. \quad (\text{B41})$$

These results allow us to define a generalized SHG phase function given by

$$\begin{aligned}
 \alpha \tilde{p}_{\text{SHG}}(\mathbf{u}, \mathbf{u}', \mathbf{u}'', \omega) &= \alpha p_{\text{SHG}}(\mathbf{u}, \mathbf{u}', \mathbf{u}'', \omega) g_{\text{SHG}}(\mathbf{r}, \mathbf{u}, \mathbf{u}', \mathbf{u}'', \omega) \\
 &= \frac{1}{125\pi^5} \check{\check{\Gamma}}_{\text{SHG}}(2k_0\mathbf{u}, k_0\mathbf{u}', k_0\mathbf{u}'', 2k_0\mathbf{u}, k_0\mathbf{u}', k_0\mathbf{u}'', \omega), \quad (\text{B42})
 \end{aligned}$$

where

$$g_{\text{SHG}}(\mathbf{r}, \mathbf{u}, \mathbf{u}', \mathbf{u}'', \omega) = \int \exp[-i\mathbf{q} \cdot \Delta] f(\mathbf{r}, \Delta) d\Delta, \quad (\text{B43})$$

in which $\mathbf{q} = k_0(2\mathbf{u} - \mathbf{u}' - \mathbf{u}'')$ is the SHG scattering vector. Substitution of the expression for the correlation function C_χ into Eq. (B35) leads to

$$p_{\text{SHG}}(\mathbf{u}, \mathbf{u}', \mathbf{u}'', \omega) \propto \exp\left[-\frac{q^2 \ell^2}{2}\right]. \quad (\text{B44})$$

We finally obtain the formulation of the RTE for the second-harmonic specific intensity linked to the second-harmonic correlation function, which reads

$$\begin{aligned} & \left[\mathbf{u} \cdot \nabla_{\mathbf{r}} + \frac{1}{\ell_s(2\omega)} \right] \tilde{I}(\mathbf{r}, \mathbf{u}, 2\omega) \\ &= \frac{1}{\ell_s(2\omega)} \int p(\mathbf{u}, \mathbf{u}', 2\omega) g(\mathbf{u}, \mathbf{u}', 2\omega) \tilde{I}(\mathbf{r}, \mathbf{u}', 2\omega) d\mathbf{u}' \\ &+ \alpha \iint p_{\text{SHG}}(\mathbf{u}, \mathbf{u}', \mathbf{u}'', \omega) g_{\text{SHG}}(\mathbf{u}, \mathbf{u}', \mathbf{u}'', \omega) \\ &\times \tilde{I}(\mathbf{r}, \mathbf{u}', \omega) \tilde{I}(\mathbf{r}, \mathbf{u}'', \omega) d\mathbf{u}' d\mathbf{u}''. \end{aligned} \quad (\text{B45})$$

The second-harmonic specific intensity is still given by the field-field correlation

$$\begin{aligned} & \delta(k - k_0) \tilde{I}(\mathbf{r}, \mathbf{u}, 2\omega) \\ &= \int \left\langle E\left(\mathbf{r} + \frac{\mathbf{s}}{2}, 2\omega\right) \tilde{E}^*\left(\mathbf{r} - \frac{\mathbf{s}}{2}, 2\omega\right) \right\rangle e^{-i\mathbf{k}\mathbf{u}\cdot\mathbf{s}} ds. \end{aligned} \quad (\text{B46})$$

This concludes the derivation of the RTE for the linear and second-harmonic beams.

APPENDIX C: VALIDITY CHECK FROM *AB INITIO* SIMULATIONS

The model developed in Appendix B is obtained under several approximations. The most important one concerns the diagrams that have to be taken into account in order to estimate the second-harmonic specific intensity. In a dilute medium, we consider that a ladder-type diagram is a leading contributor to the second-harmonic speckle correlation. In order to check the validity of this approximation, we run *ab initio* simulations of Maxwell equations using a coupled-dipole formalism and compare the results to the RTE model solved using a Monte Carlo scheme.

It is important to note that we consider here a simplified model that does not reflect the conditions of the experiment but that helps to check the validity of the transport model. In particular, the coupled-dipole formalism used

here implies that the disorder model is limited to point scatterers randomly located inside the medium. Regarding the scatterer displacement model, we simply consider that a scatterer can move in an arbitrary direction over a distance d that is fixed.

Moreover, the numerical resolution of Maxwell equations requires significant computing resources. This is the reason why we restrict to two-dimensional (2D) systems in TE polarization (electric field along the direction of invariance by translation). This means that a scalar model can be used and no polarization effects have to be taken into account.

1. Coupled-dipole model

a. Linear regime

In the linear regime, the coupled-dipole equations are given by

$$E_i(\omega) = E_0(\mathbf{r}_i, \omega) + k_0^2 \alpha(\omega) \sum_{\substack{j=1 \\ j \neq i}}^N G_0(\mathbf{r}_i - \mathbf{r}_j, \omega) E_j(\omega), \quad (\text{C1})$$

$$E(\mathbf{r}, \omega) = E_0(\mathbf{r}, \omega) + k_0^2 \alpha(\omega) \sum_{j=1}^N G_0(\mathbf{r} - \mathbf{r}_j, \omega) E_j(\omega). \quad (\text{C2})$$

E_i represents the field illuminating the scatterer i lying at position \mathbf{r}_i . It is also called the exciting field. It is given by two contributions: the incident field E_0 and the field scattered by all other scatterers. $G_0(\mathbf{r} - \mathbf{r}_0, \omega)$ is the Green function in vacuum. It links the field created at position \mathbf{r} by a source dipole $p(\omega)$ lying at position \mathbf{r}_0 through the relation

$$E(\mathbf{r}, \omega) = \mu_0 \omega^2 G_0(\mathbf{r} - \mathbf{r}_0, \omega) p(\omega). \quad (\text{C3})$$

For 2D TE waves, it is given by

$$G_0(\mathbf{R}, \omega) = \frac{i}{4} H_0^{(1)}(k_0 |\mathbf{R}|), \quad (\text{C4})$$

where $H_0^{(1)}$ is the Hankel function of the first kind and zero order. $\alpha(\omega)$ is the polarizability of the scatterer, which describes the optical response of the particle. In the nonabsorbing case, energy conservation implies

$$k_0 \text{Im} \alpha(\omega) = \frac{k_0^3}{4} |\alpha(\omega)|^2. \quad (\text{C5})$$

Once the exciting fields have been computed for all dipoles by solving the set of Eqs. (C1), the field at any position, i.e., $E(\mathbf{r}, \omega)$, can be computed using Eq. (C2).

In order to take scatterer displacements into account, we just have to redo the same computation after moving the scatterers by a distance d in arbitrary directions. Then we have access to $\tilde{E}(\mathbf{r}, \omega)$. An average over several disorder configurations allows estimation of the correlation function:

$$c_{\text{CD}}(\mathbf{r}, \omega) = \frac{\langle E(\mathbf{r}, \omega) \tilde{E}^*(\mathbf{r}, \omega) \rangle}{\langle E(\mathbf{r}, \omega) E^*(\mathbf{r}, \omega) \rangle}, \quad (\text{C6})$$

where the subscript ‘‘CD’’ means ‘‘coupled dipoles.’’

b. Nonlinear regime

The second-harmonic regime is still considered through the standard perturbative approach. This means that the coupled-dipole equations are written as follows:

$$E_i(2\omega) = \frac{\beta}{\alpha(2\omega)} E_i(\omega)^2 + k_0^2 \alpha(2\omega) \sum_{\substack{j=1 \\ j \neq i}}^N G_0(\mathbf{r}_i - \mathbf{r}_j, 2\omega) E_j(2\omega), \quad (\text{C7})$$

$$E(\mathbf{r}, 2\omega) = k_0^2 \alpha(2\omega) \sum_{j=1}^N G_0(\mathbf{r} - \mathbf{r}_j, 2\omega) E_j(2\omega), \quad (\text{C8})$$

where β can be seen as a second-harmonic polarizability. This set of equations is solved using the results of the linear case and following exactly the same steps. This leads to an estimate of the correlation function:

$$c_{\text{CD}}(\mathbf{r}, 2\omega) = \frac{\langle E(\mathbf{r}, 2\omega) \tilde{E}^*(\mathbf{r}, 2\omega) \rangle}{\langle E(\mathbf{r}, 2\omega) E^*(\mathbf{r}, 2\omega) \rangle}. \quad (\text{C9})$$

2. Monte Carlo scheme

In order to solve the set of transport equations, we perform Monte Carlo simulations. For a cloud of uncorrelated point dipoles lying in a 2D dilute medium and considering TE waves, the parameters are given by

$$\ell_s(\omega) = \frac{1}{\rho \sigma_s(\omega)}, \quad \text{where} \quad \sigma_s(\omega) = \frac{k_0^3}{4} |\alpha(\omega)|^2, \quad (\text{C10})$$

$$p(\mathbf{u}, \mathbf{u}', \omega) = \frac{1}{2\pi}, \quad p_{\text{SHG}}(\mathbf{u}, \mathbf{u}', \mathbf{u}'', \omega) = \frac{1}{4\pi^2}, \quad (\text{C11})$$

and

$$f(\mathbf{r}, \mathbf{\Delta}) = \frac{\delta(\Delta - d)}{2\pi \Delta}, \quad (\text{C12})$$

ρ being the density of the scatterers. Two different Monte Carlo simulations are done. The first one solves Eq. (B30).

This is a fully standard Monte Carlo scheme except that we have to multiply the energy quanta of the random-walk packets by $g(\mathbf{r}, \mathbf{u}, \mathbf{u}', \omega)$ at each scattering event in order to take the decorrelation process into account. At the end, we have access to a map of the specific intensity $\tilde{I}(\mathbf{r}, \mathbf{u}, \omega)$, which is used to compute the correlation function

$$c_{\text{MC}}(\mathbf{r}, \omega) = \frac{\int \tilde{I}(\mathbf{r}, \mathbf{u}, \omega) d\mathbf{u}}{\int I(\mathbf{r}, \mathbf{u}, \omega) d\mathbf{u}}, \quad (\text{C13})$$

where the subscript ‘‘MC’’ means ‘‘Monte Carlo.’’ The second Monte Carlo simulation is used to solve Eq. (B45) and is similar to the first one except that the source term is given by the SHG process [the last term of Eq. (B45)]. At the end, we have access to the specific intensity $\tilde{I}(\mathbf{r}, \mathbf{u}, 2\omega)$, which gives the correlation function

$$c_{\text{MC}}(\mathbf{r}, 2\omega) = \frac{\int \tilde{I}(\mathbf{r}, \mathbf{u}, 2\omega) d\mathbf{u}}{\int I(\mathbf{r}, \mathbf{u}, 2\omega) d\mathbf{u}}. \quad (\text{C14})$$

3. Comparison of numerical results

To make comparisons between the couple-dipole formalism and the Monte Carlo simulations, we consider a slab geometry of thickness L illuminated by a plane wave at normal incidence, as represented in Fig. 9(b). However, this very simple model has to be slightly adapted in the case of the coupled-dipole simulation, which is detailed in Fig. 9(a). Indeed, the finite number of scatterers imposes a finite transverse size D . Moreover, in order to avoid diffraction effects at the transverse boundaries, we choose

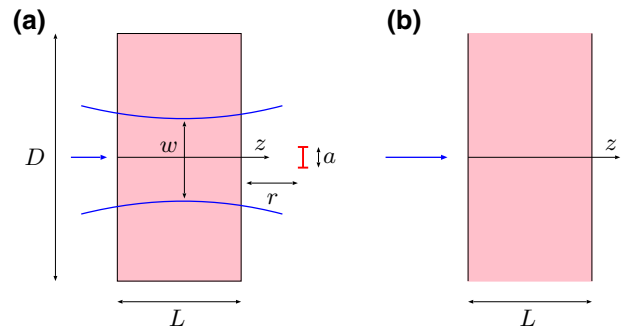


FIG. 9. The 2D slab geometry considered to validate the transport approach. (a) The scattering rectangle used in the coupled-dipole simulation. We have $D \gg \{L, w\}$ and $w \gg \{L, \lambda\}$ to mimic a slab geometry illuminated by a plane wave at normal incidence. a is the transverse size of the detection zone, where we compute the correlation functions \mathcal{C} . We have $w \gg a \gg \lambda$ to capture several speckle grains in order to improve the statistical convergence. We also have $r > \lambda$ to avoid near-field interaction close to the interface. (b) The infinite scattering slab used in the Monte Carlo simulation. Since the *ab initio* computation is done using point dipoles, the standard phase function p as well as the SHG phase function p_{SHG} are chosen to be isotropic ($g = 0$).

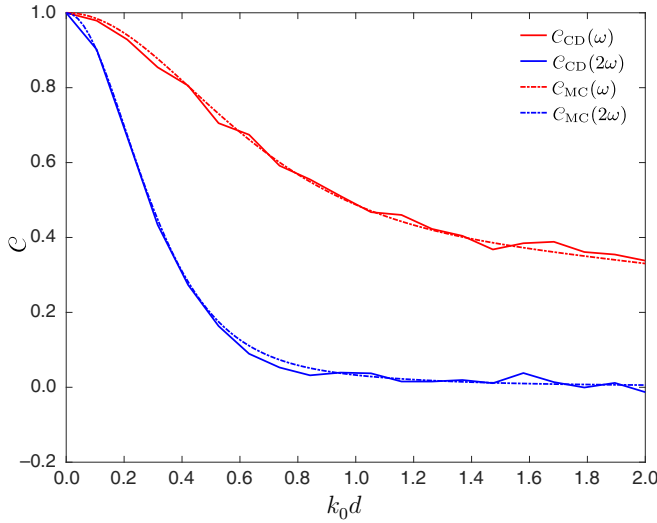


FIG. 10. A comparison of the correlation functions obtained using the coupled-dipole simulations (C_{CD}) and the Monte Carlo schemes (C_{MC}) for the linear (ω) and second-harmonic (2ω) beams as a function of the normalized displacement distance k_0d . The parameters are $k_0L = 100$, $k_0D = 8000$, $k_0/\sqrt{\rho} = 6$, $k_0w = 3800$, $k_0r = 5$, and $k_0a = 8$. The polarizability is chosen such that $k_0\ell_s(\omega) = 50$ and $k_0\ell_s(2\omega) = 50$, which leads to $b(\omega) = b(2\omega) = 2$. $N_c = 256$ configurations are used for the coupled-dipole simulations and $N_p = 5 \times 10^6$ random-walk packets are used for the Monte Carlo schemes.

to illuminate the medium by a Gaussian beam of waist w . We choose $D \gg \{L, w\}$ and $w \gg \{L, \lambda\}$. The speckle correlation functions are computed just behind the slab, at a distance r from the interface and averaged along a transverse distance a in the case of the coupled-dipole simulation. In the case of the Monte Carlo simulation, we consider the full transmitted specific intensity.

We test several sets of parameters, each of which gives rise to very good agreement between the results of the two numerical approaches. This proves that the theoretical model is accurate and that the diagram considered for the second-harmonic correlation function is the leading term. As an example, we show in Fig. 10 the results for an optical thickness $b = L/\ell_s = 2$ for both the linear and second-harmonic beams.

APPENDIX D: DIFFUSION LIMIT

This appendix is devoted to obtaining analytical expressions of the correlation functions in the diffusion limit. We consider a three-dimensional slab geometry of thickness L illuminated by a plane wave at normal incidence. This implies that all physical quantities will depend only on the depth z inside the medium. The diffusion approximation requires that $L \gg \{\ell_t(\omega), \ell_t(2\omega)\}$, ℓ_t being the transport mean free path. We also assume that the displacement

direction of the scatterers is isotropic, which leads to

$$f(\mathbf{r}, \Delta) = \frac{f(\Delta)}{4\pi\Delta^2}. \quad (\text{D1})$$

1. Linear regime

We first consider the linear regime. Defining the absorption length $\tilde{\ell}_a$ and the anisotropy factor \tilde{g} by

$$\begin{aligned} \frac{1}{\tilde{\ell}_a(\omega)} &= \frac{1}{\tilde{\ell}_e(\omega)} - \frac{1}{\tilde{\ell}_s(\omega)} \\ &= \frac{1}{\tilde{\ell}_s(\omega)} \left[1 - \int p(\mathbf{u}, \mathbf{u}', \omega) g(\mathbf{u}, \mathbf{u}', \omega) d\mathbf{u}' \right], \end{aligned} \quad (\text{D2})$$

$$\begin{aligned} \tilde{g}(\omega) &= \frac{1}{\tilde{\ell}_s(\omega)} \int \tilde{p}(\mathbf{u}, \mathbf{u}', \omega) \mathbf{u} \cdot \mathbf{u}' d\mathbf{u}' \\ &= \frac{\int p(\mathbf{u}, \mathbf{u}', \omega) g(\mathbf{u}, \mathbf{u}', \omega) \mathbf{u} \cdot \mathbf{u}' d\mathbf{u}'}{\int p(\mathbf{u}, \mathbf{u}', \omega) g(\mathbf{u}, \mathbf{u}', \omega) d\mathbf{u}'}, \end{aligned} \quad (\text{D3})$$

we are back to the standard RTE with an absorption term. Thus we can apply the no less standard diffusion-equation derivation in the framework of the P1 approximation [1]. Since the diffusion equation is valid only for the diffuse part of the correlation function, we split it into its ballistic (C_b) and diffuse (C_d) components, which gives

$$\begin{aligned} C(\mathbf{r}, \omega) &= \langle E(\mathbf{r}, \omega) \rangle \langle \tilde{E}^*(\mathbf{r}, \omega) \rangle + \langle \delta E(\mathbf{r}, \omega) \delta \tilde{E}^*(\mathbf{r}, \omega) \rangle \\ &= C_b(\mathbf{r}, \omega) + C_d(\mathbf{r}, \omega). \end{aligned} \quad (\text{D4})$$

This splitting is similar to the one that we usually perform on the average intensity. The ballistic component is given by

$$C_b(z, \omega) = I_0 \exp[-z/\ell_s(\omega)] \quad (\text{D5})$$

and its diffuse counterpart reads

$$\begin{aligned} &\left[-\frac{\tilde{\ell}_s(\omega)\tilde{\ell}_t(\omega)}{3} \frac{\partial^2}{\partial z^2} + \frac{\tilde{\ell}_s(\omega)}{\tilde{\ell}_a(\omega)} \right] C_d(z, \omega) \\ &= \frac{1}{1 - \tilde{g}(\omega)} C_b(z, \omega), \end{aligned} \quad (\text{D6})$$

where the transport mean free path is given by

$$\tilde{\ell}_t(\omega) = \frac{\tilde{\ell}_s(\omega)}{1 - \tilde{g}(\omega)}. \quad (\text{D7})$$

The boundary conditions involve the standard extrapolation length $\tilde{z}_0(\omega) = 2\tilde{\ell}_t(\omega)/3$ and are given by

$$C_d(z=0, \omega) - \tilde{z}_0(\omega) \frac{\partial C_d}{\partial z}(z=0, \omega) = -\frac{2\tilde{g}(\omega)}{1 - \tilde{g}(\omega)} C_b(z=0, \omega), \quad (\text{D8})$$

$$C_d(z=L, \omega) + \tilde{z}_0(\omega) \frac{\partial C_d}{\partial z}(z=L, \omega) = \frac{2\tilde{g}(\omega)}{1 - \tilde{g}(\omega)} C_b(z=L, \omega). \quad (\text{D9})$$

The resolution of this set of equations is straightforward. Using the fact that $\ell_s \ll L$, an approximate solution is given by

$$C_d(z, \omega) = \left[-2 \frac{g(\omega)}{1 - g(\omega)} + 3 \left\{ 1 + \frac{z_0(\omega)}{\ell_s(\omega)} \right\} \right] \times I_0 \frac{\sinh[\kappa(\omega)(L - z)]}{\sinh[\kappa(\omega)L]} = 5I_0 \frac{\sinh[\kappa(\omega)(L - z)]}{\sinh[\kappa(\omega)L]}. \quad (\text{D10})$$

Thus, close to the output interface in transmission, the normalized correlation is given by

$$C_d(z=L, \omega) = \frac{\kappa(\omega)L}{\sinh[\kappa(\omega)L]}, \quad (\text{D11})$$

where

$$\kappa(\omega) = \sqrt{\frac{3}{\tilde{\ell}_t(\omega)\tilde{\ell}_a(\omega)}}. \quad (\text{D12})$$

Equation (D11) is the standard expression that we usually obtain in the case of a large absorbing scattering medium, except that here, the usual absorption term describes a decorrelation process.

2. Second-harmonic regime

We now move to the second-harmonic regime and we have to apply the standard diffusion-equation derivation to the nonlinear RTE given by Eq. (B45). Since the goal of this appendix is to obtain analytical results, we first have to make an assumption on the specific intensity at frequency ω that enters the source term in the nonlinear RTE. Deeply inside the medium, we consider that its diffuse part

is isotropic, which gives

$$\tilde{I}(\mathbf{r}, \mathbf{u}, \omega) = C_b(z, \omega)\delta(\mathbf{u} - \mathbf{e}_z) + \frac{C_d(z, \omega)}{4\pi}. \quad (\text{D13})$$

The correlation at 2ω is still given by

$$C(\mathbf{r}, 2\omega) = \langle E(\mathbf{r}, 2\omega) \rangle \langle \tilde{E}^*(\mathbf{r}, 2\omega) \rangle + \langle \delta E(\mathbf{r}, 2\omega) \delta \tilde{E}^*(\mathbf{r}, 2\omega) \rangle = C_b(\mathbf{r}, 2\omega) + C_d(\mathbf{r}, 2\omega). \quad (\text{D14})$$

The ballistic component can be fully neglected. Indeed, it corresponds to a diagram where both the SHG processes for the field and its conjugate take place in statistically independent positions. This implies that phase matching cannot be obtained and this term vanishes. Besides, it is important to note that this diagram is not taken into account in Eq. (B45). In order to obtain a diffusion equation for the diffuse component, we first define the first and second moments of the SHG phase function by

$$m_0(z, \omega) = \int S(z, \mathbf{u}, \omega) d\mathbf{u},$$

$$m_1(z, \omega) = \int S(z, \mathbf{u}, \omega) \mathbf{u} \cdot \mathbf{e}_z d\mathbf{u}, \quad (\text{D15})$$

where S is the source term of the RTE at 2ω , given by

$$S(z, \mathbf{u}, \omega) = \alpha \iint p_{\text{SHG}}(\mathbf{u}, \mathbf{u}', \mathbf{u}'', \omega) g_{\text{SHG}}(\mathbf{u}, \mathbf{u}', \mathbf{u}'', \omega) \times \tilde{I}(\mathbf{r}, \mathbf{u}', \omega) \tilde{I}(\mathbf{r}, \mathbf{u}'', \omega) d\mathbf{u}' d\mathbf{u}''. \quad (\text{D16})$$

Then, we obtain the diffusion equation for the diffuse component, given by

$$\left[-\frac{\tilde{\ell}_s(2\omega)\tilde{\ell}_t(2\omega)}{3} \frac{\partial^2}{\partial z^2} + \frac{\tilde{\ell}_s(2\omega)}{\tilde{\ell}_a(2\omega)} \right] C_d(z, 2\omega) = \tilde{\ell}_s(2\omega)m_0(z, \omega) - \tilde{\ell}_s(2\omega)\tilde{\ell}_t(2\omega) \frac{\partial}{\partial z} m_1(z, \omega), \quad (\text{D17})$$

with the boundary conditions

$$C_d(z=0, 2\omega) - \tilde{z}_0(2\omega) \frac{\partial C_d}{\partial z}(z=0, 2\omega) = -\frac{2\tilde{\ell}_s(2\omega)m_1(z=0, \omega)}{1 - \tilde{g}(2\omega)}, \quad (\text{D18})$$

$$C_d(z=L, 2\omega) + \tilde{z}_0(2\omega) \frac{\partial C_d}{\partial z}(z=L, 2\omega) = \frac{2\tilde{\ell}_s(2\omega)m_1(z=L, \omega)}{1 - \tilde{g}(2\omega)}. \quad (\text{D19})$$

Writing S in the form

$$\begin{aligned} S(z, \mathbf{u}, \omega) &= \alpha C_b(z, \omega)^2 \mathcal{A}(\mathbf{u}, \omega) \\ &+ \frac{\alpha}{4\pi} C_b(z, \omega) C_d(z, \omega) \mathcal{B}(\mathbf{u}, \omega) \\ &+ \frac{\alpha}{16\pi^2} C_d(z, \omega)^2 \mathcal{C}(\mathbf{u}, \omega), \end{aligned} \quad (\text{D20})$$

where

$$\mathcal{A}(\mathbf{u}, \omega) = p_{\text{SHG}}(\mathbf{u}, \mathbf{e}_z, \mathbf{e}_z, \omega) g_{\text{SHG}}(\mathbf{u}, \mathbf{e}_z, \mathbf{e}_z, \omega), \quad (\text{D21})$$

$$\begin{aligned} \mathcal{B}(\mathbf{u}, \omega) &= \frac{1}{4\pi} \int p_{\text{SHG}}(\mathbf{u}, \mathbf{u}', \mathbf{e}_z, \omega) g_{\text{SHG}}(\mathbf{u}, \mathbf{u}', \mathbf{e}_z, \omega) \\ &+ p_{\text{SHG}}(\mathbf{u}, \mathbf{e}_z, \mathbf{u}', \omega) g_{\text{SHG}}(\mathbf{u}, \mathbf{e}_z, \mathbf{u}', \omega) d\mathbf{u}', \end{aligned} \quad (\text{D22})$$

and

$$\begin{aligned} \mathcal{C}(\mathbf{u}, \omega) &= \frac{1}{16\pi^2} \iint p_{\text{SHG}}(\mathbf{u}, \mathbf{u}', \mathbf{u}'', \omega) \\ &\times g_{\text{SHG}}(\mathbf{u}, \mathbf{u}', \mathbf{u}'', \omega) d\mathbf{u}' d\mathbf{u}'', \end{aligned} \quad (\text{D23})$$

we obtain

$$\begin{aligned} m_0(z, \omega) &= \alpha \left[C_b(z, \omega)^2 \mathcal{A}_0(\omega) \right. \\ &+ \frac{1}{4\pi} C_b(z, \omega) C_d(z, \omega) \mathcal{B}_0(\omega) \\ &+ \left. \frac{1}{16\pi^2} C_d(z, \omega)^2 \mathcal{C}_0(\omega) \right], \end{aligned} \quad (\text{D24})$$

$$\begin{aligned} m_1(z, \omega) &= \alpha \left[C_b(z, \omega)^2 \mathcal{A}_1(\omega) \right. \\ &+ \frac{1}{4\pi} C_b(z, \omega) C_d(z, \omega) \mathcal{B}_1(\omega) \\ &+ \left. \frac{1}{16\pi^2} C_d(z, \omega)^2 \mathcal{C}_1(\omega) \right], \end{aligned} \quad (\text{D25})$$

with

$$\mathcal{X}_0(\omega) = \int \mathcal{X}(\mathbf{u}, \omega) d\mathbf{u}, \quad \mathcal{X}_1(\omega) = \int \mathcal{X}(\mathbf{u}, \omega) \mathbf{u} \cdot \mathbf{e}_z d\mathbf{u}, \quad (\text{D26})$$

where $\mathcal{X} = \mathcal{A}, \mathcal{B}, \mathcal{C}$. Since we consider that the diffusive regime is valid, in the following we neglect the ballistic component C_b . Thus $\mathcal{A} \sim 0$ and $\mathcal{B} \sim 0$. Moreover, \mathcal{C} is of the form

$$\begin{aligned} \mathcal{C}(\mathbf{u}, \omega) &= \frac{1}{16\pi^2} \\ &\times \iint F(6 - 4\mathbf{u} \cdot \mathbf{u}' - 4\mathbf{u} \cdot \mathbf{u}'' + 2\mathbf{u}' \cdot \mathbf{u}'', \omega) \\ &\times d\mathbf{u}' d\mathbf{u}'', \end{aligned} \quad (\text{D27})$$

which implies that \mathcal{C} is independent of \mathbf{u} . This leads to $\mathcal{C}_1 = 0$. Finally, only \mathcal{C}_0 is nonzero. In order to compute $C_d(z, 2\omega)$, we note that

$$\begin{aligned} C_d(z, \omega)^2 &= \frac{25I_0^2}{2 \sinh[\kappa(\omega)L]^2} \\ &\times [e^{2\kappa(\omega)(L-z)} + e^{-2\kappa(\omega)(L-z)} - 2]. \end{aligned} \quad (\text{D28})$$

Thus the diffusion equation becomes

$$\begin{aligned} &\left[-\frac{\tilde{\ell}_s(2\omega)\tilde{\ell}_l(2\omega)}{3} \frac{\partial^2}{\partial z^2} + \frac{\tilde{\ell}_s(2\omega)}{\tilde{\ell}_a(2\omega)} \right] C_d(z, 2\omega) \\ &= \frac{25I_0\tilde{\ell}_s(2\omega)\alpha C_0(\omega)}{32\pi^2 \sinh[\kappa(\omega)L]^2} [e^{2\kappa(\omega)(L-z)} + e^{-2\kappa(\omega)(L-z)} - 2], \end{aligned} \quad (\text{D29})$$

with the boundary conditions

$$C_d(z=0, 2\omega) - \tilde{z}_0(2\omega) \frac{\partial C_d}{\partial z}(z=0, 2\omega) = 0, \quad (\text{D30})$$

$$C_d(z=L, 2\omega) + \tilde{z}_0(2\omega) \frac{\partial C_d}{\partial z}(z=L, 2\omega) = 0. \quad (\text{D31})$$

The resolution of this set of equations is still straightforward and we obtain

$$\begin{aligned} C_d(z=L, 2\omega) &= \frac{6\mathcal{D}(\omega)}{\kappa(2\omega)L \sinh[\kappa(\omega)L]^2 \sinh[\kappa(2\omega)L]} \\ &\times \frac{\kappa(2\omega)^2 \{1 - \cosh[2\kappa(\omega)L]\} - 4\kappa(\omega)^2 \{1 - \cosh[\kappa(2\omega)L]\}}{\kappa(2\omega)^2 - 4\kappa(\omega)^2}, \end{aligned} \quad (\text{D32})$$

where

$$\mathcal{D}(\omega) = \frac{1}{4\pi} \int p_{\text{SHG}}(\mathbf{u}, \mathbf{u}', \mathbf{u}'', \omega) g_{\text{SHG}}(\mathbf{u}, \mathbf{u}', \mathbf{u}'', \omega) \times d\mathbf{u}d\mathbf{u}'d\mathbf{u}'' \quad (\text{D33})$$

In this expression, we define

$$\kappa(2\omega) = \sqrt{\frac{3}{\tilde{\ell}_t(2\omega)\tilde{\ell}_a(2\omega)}} \quad (\text{D34})$$

In the particular case where $\kappa(2\omega) = 2\kappa(\omega)$, we obtain

$$C_d(z=L, 2\omega) = \frac{3\mathcal{D}(\omega)}{\sinh[\kappa(\omega)L]} \times \left[\frac{1}{\sinh[\kappa(\omega)L]} - \frac{1}{\kappa(\omega)L \cosh[\kappa(\omega)L]} \right] \quad (\text{D35})$$

3. Comparison to Monte Carlo simulations

In order to check the validity of Eqs. (D11) and (D32), we perform Monte Carlo simulations in the particular case of a constant displacement amplitude d such that $k_0d \ll 1$ and $f(\Delta) = \delta(\Delta - d)$. This gives

$$\kappa(\omega)L = b(\omega)k_0d, \quad \kappa(2\omega)L = 2b(2\omega)k_0d, \quad (\text{D36})$$

$$\text{and } \mathcal{D}(\omega) = \frac{1}{8\pi} \int_{\phi=0}^{2\pi} \int_{\mu=-1}^1 \int_{\mu'=-1}^1 \text{sinc} \left[k_0d \sqrt{6 - 4\mu - 4\mu' + 2\mu\mu' + 2\sqrt{1-\mu^2}\sqrt{1-\mu'^2} \cos \phi} \right] d\mu d\mu' d\phi \quad (\text{D37})$$

An example of the results obtained is reported in Fig. 11 for $b(\omega) = b(2\omega) = 40$, $g(\omega) = 0.31$, and $g(2\omega) = 0.75$. The disorder correlation is given by $k_0\ell = 1$. Good agreement is obtained.

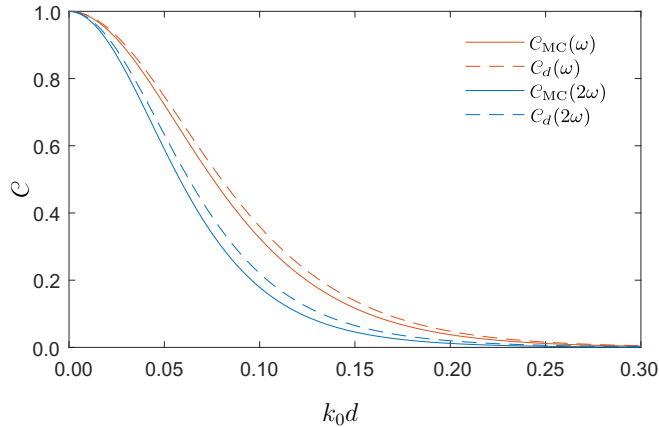


FIG. 11. A comparison of the correlation functions obtained using the Monte Carlo scheme (C_{MC}) and the diffusion approximation (C_d) for the linear (ω) and second-harmonic (2ω) beams as a function of the normalized displacement distance k_0d . The parameters are $b(\omega) = b(2\omega) = 40$, $g(\omega) = 0.31$, $g(2\omega) = 0.75$, and $k_0\ell = 1$. $N_p = 28 \times 10^6$ random-walk packets are used for the Monte Carlo schemes.

- [1] A. Ishimaru, *Wave Propagation and Scattering in Random Media* (IEEE Press, Oxford, 1997).
- [2] D. S. Wiersma, Disordered photonics, *Nat. Photonics* **7**, 188 (2013).
- [3] C. Conti, L. Angelani, and G. Ruocco, Light diffusion and localization in three-dimensional nonlinear disordered media, *Phys. Rev. A* **75**, 033812 (2007).
- [4] I. V. Shadrivov, K. Y. Bliokh, Y. P. Bliokh, V. Freilikher, and Y. S. Kivshar, Bistability of Anderson Localized States in Nonlinear Random Media, *Phys. Rev. Lett.* **104**, 123902 (2010).
- [5] A. Mafi, A brief overview of the interplay between nonlinearity and transverse Anderson localization (2017), [ArXiv:1703.04011](https://arxiv.org/abs/1703.04011).
- [6] Y. Sharabi, H. H. Sheinfux, Y. Sagi, G. Eisenstein, and M. Segev, Self-Induced Diffusion in Disordered Nonlinear Photonic Media, *Phys. Rev. Lett.* **121**, 233901 (2018).
- [7] V. M. Agranovich and V. E. Kravtsov, Effects of weak localization of photons in nonlinear optics: Second harmonic generation, *Phys. Lett. A* **131**, 378 (1988).
- [8] K. M. Yoo, S. Lee, Y. Takiguchi, and R. R. Alfano, Search for the effect of weak photon localization in second-harmonic waves generated in a disordered anisotropic nonlinear medium, *Opt. Lett.* **14**, 800 (1989).
- [9] E. V. Makeev and S. E. Skipetrov, Second harmonic generation in suspensions of spherical particles, *Opt. Commun.* **224**, 139 (2003).
- [10] S. Faez, P. M. Johnson, D. A. Mazurenko, and A. Lagendijk, Experimental observation of second-harmonic

- generation and diffusion inside random media, *J. Opt. Soc. Am. B* **26**, 235 (2009).
- [11] C. I. Valencia and E. R. Méndez, Weak localization effects in the second-harmonic light scattered by random systems of particles, *Opt. Commun.* **282**, 1706 (2009).
- [12] R. Savo, A. Morandi, J. S. Müller, F. Kaufmann, F. Timpu, M. R. Escalé, M. Zanini, L. Isa, and R. Grange, Broadband mie driven random quasi-phase-matching, *Nat. Photonics* **14**, 740 (2020).
- [13] J. S. Müller, A. Morandi, R. Grange, and R. Savo, Modeling of Random Quasi-Phase-Matching in Birefringent Disordered Media, *Phys. Rev. Appl.* **15**, 064070 (2021).
- [14] A. Morandi, R. Savo, J. S. Müller, S. Reichen, and R. Grange, Multiple scattering and random quasi-phase-matching in disordered assemblies of LiNbO₃ nanocubes, *ACS Photonics* **9**, 1882 (2022).
- [15] J. W. Goodman, *Speckle Phenomena in Optics: Theory and Applications* (Roberts & Company, Englewood, 2007).
- [16] S. Feng, C. Kane, P. A. Lee, and A. D. Stone, Correlations and Fluctuations of Coherent Wave Transmission through Disordered Media, *Phys. Rev. Lett.* **61**, 834 (1988).
- [17] I. Freund, M. Rosenbluh, and S. Feng, Memory Effects in Propagation of Optical Waves through Disordered Media, *Phys. Rev. Lett.* **61**, 2328 (1988).
- [18] S. Schott, J. Bertolotti, J.-F. Léger, L. Bourdieu, and S. Gigan, Characterization of the angular memory effect of scattered light in biological tissues, *Opt. Exp.* **23**, 13505 (2015).
- [19] B. Judkewitz, R. Horstmeyer, I. M. Vellekoop, I. N. Papadopoulos, and C. Yang, Translation correlations in anisotropically scattering media, *Nat. Phys.* **11**, 684 (2015).
- [20] G. Osnabrugge, R. Horstmeyer, I. N. Papadopoulos, B. Judkewitz, and I. M. Vellekoop, Generalized optical memory effect, *Optica* **4**, 886 (2017).
- [21] H. Liu, Z. Liu, M. Chen, S. Han, and L. V. Wang, Physical picture of the optical memory effect, *Photonics Res.* **7**, 1323 (2019).
- [22] J. Bertolotti, E. G. van Putten, C. Blum, A. Lagendijk, W. L. Vos, and A. P. Mosk, Non-invasive imaging through opaque scattering layers, *Nature* **491**, 232 (2012).
- [23] O. Katz, P. Heidmann, M. Fink, and S. Gigan, Non-invasive single-shot imaging through scattering layers and around corners via speckle correlations, *Nat. Photonics* **8**, 784 (2014).
- [24] N. Fayard, A. Cazé, R. Pierrat, and R. Carminati, Intensity correlations between reflected and transmitted speckle patterns, *Phys. Rev. A* **92**, 033827 (2015).
- [25] N. Fayard, A. Goetschy, R. Pierrat, and R. Carminati, Mutual Information between Reflected and Transmitted Speckle Images, *Phys. Rev. Lett.* **120**, 073901 (2018).
- [26] I. Starshynov, A. M. Paniagua-Diaz, N. Fayard, A. Goetschy, R. Pierrat, R. Carminati, and J. Bertolotti, Non-Gaussian Correlations between Reflected and Transmitted Intensity Patterns Emerging from Opaque Disordered Media, *Phys. Rev. X* **8**, 021041 (2018).
- [27] A. Fleming, C. Conti, T. Vettenburg, and A. D. Falco, Non-linear optical memory effect, *Opt. Lett.* **44**, 4841 (2019).
- [28] S. E. Skipetrov and R. Maynard, Instabilities of Waves in Nonlinear Disordered Media, *Phys. Rev. Lett.* **85**, 736 (2000).
- [29] S. E. Skipetrov, Instability of speckle patterns in random media with noninstantaneous Kerr nonlinearity, *Opt. Lett.* **28**, 646 (2003).
- [30] S. E. Skipetrov, Dynamic instability of speckle patterns in nonlinear random media, *J. Opt. Soc. Am. B* **21**, 168 (2004).
- [31] B. Grémaud and T. Wellens, Speckle Instability: Coherent Effects in Nonlinear Disordered Media, *Phys. Rev. Lett.* **104**, 133901 (2010).
- [32] I. I. Smolyaninov, A. Gungor, and C. C. Davis, Experimental observation of speckle instability in a two-dimensional disordered medium, *Metamaterials* **4**, 207 (2010).
- [33] J. F. de Boer, A. Lagendijk, R. Sprik, and S. Feng, Transmission and Reflection Correlations of Second Harmonic Waves in Nonlinear Random Media, *Phys. Rev. Lett.* **71**, 3947 (1993).
- [34] T. Ito and M. Tomita, Speckle correlation measurement in a disordered medium observed through second-harmonics generation, *Phys. Rev. E* **69**, 036610 (2004).
- [35] P.-E. Wolf and G. Maret, Weak Localization and Coherent Backscattering of Photons in Disordered Media, *Phys. Rev. Lett.* **55**, 2696 (1985).
- [36] E. Akkermans, P. E. Wolf, and R. Maynard, Coherent Backscattering of Light by Disordered Media: Analysis of the Peak Line Shape, *Phys. Rev. Lett.* **56**, 1471 (1986).
- [37] R. Samanta and S. Mujumdar, Intensity-dependent speckle contrast of second harmonic light in a nonlinear disordered medium, *Appl. Opt.* **59**, 11266 (2020).
- [38] S. E. Skipetrov, S. S. Chesnokov, S. D. Zakharov, M. A. Kazaryan, and V. A. Shcheglov, Ponderomotive action of light in the problem of multiple scattering of light in a randomly inhomogeneous medium, *J. Exp. Theor. Phys. Lett.* **67**, 635 (1998).
- [39] K. Vynck, R. Pierrat, and R. Carminati, Polarization and spatial coherence of electromagnetic waves in uncorrelated disordered media, *Phys. Rev. A* **89**, 013842 (2014).
- [40] R. Pierrat, Transport equation for the time correlation function of scattered field in dynamic turbid media, *J. Opt. Soc. Am. A* **25**, 2840 (2008).
- [41] D. V. Kupriyanov, I. M. Sokolov, and M. D. Havey, Mesoscopic coherence in light scattering from cold, optically dense and disordered atomic systems, *Phys. Rep.* **671**, 1 (2017).
- [42] S. M. Rytov, Y. A. Kravtsov, and V. I. Tatarskii, *Principles of Statistical Radiophysics* Vol. 4 (Springer-Verlag, Berlin, 1989).
- [43] S. Chandrasekhar, *Radiative Transfer* (Dover, New York, 1950).
- [44] R. Siegel and J. R. Howell, *Thermal Radiation Heat Transfer* (Hemisphere, Washington, DC, 1992), 3rd ed.
- [45] L. A. Apresyan and Y. A. Kravtsov, *Radiation Transfer: Statistical and Wave Aspects* (Gordon and Breach, Amsterdam, 1996).
- [46] M. C. W. van Rossum and T. M. Nieuwenhuizen, Multiple scattering of classical waves: Microscopy, mesoscopy and diffusion, *Rev. Mod. Phys.* **71**, 313 (1999).
- [47] R. Pierrat, R. Carminati, and J.-L. Le Gouët, Photon echoes in strongly scattering media: A diagrammatic approach, *Phys. Rev. A* **97**, 063816 (2018).